Topological edge states in the 1/5-depleted square lattice

Tianqi Chen

Condensed Matter Theory, Department of Theoretical Physics,
School of Engineering Sciences
Royal Institute of Technology, SE-106 91 Stockholm, Sweden

Typeset in LaTeX

Cover illustration: The quantum wave image taken from *A. Yazdani*'s website at Princeton University. Originated from *P. Roushan* et al., 2009.

And I seek not mine own glory: there is one that seeketh and judgeth. (John 8:50)

Abstract

In recent years, there has been great interest in the study of topological insulators. A topological insulator is a material with non-trivial topological order that behaves as an insulator in its interior but has conducting states, where electrons can move freely. In this thesis, we present a study of the topological edge states of one particular model: the $\frac{1}{5}$-depleted square lattice model. We extend earlier work on this model from the perspective of topological insulators within the framework of band structure theory. First we briefly review several main topics in two-dimensional topological insulators and topological edge states such as the Berry curvature of Bloch states in the Brillouin zone and the (spin) Chern number. The model is based on the tight-binding formalism that is also reviewed briefly. We add both intrinsic and Rashba spin-orbit coupling into the Hamiltonian and found out how it will relieve the degeneracies around the highly symmetric Dirac points in the band structure. The Dirac-like equation that allows for an analytic calculation of the Berry curvature is obtained using the $\mathbf{k} \cdot \mathbf{p}$ method and the edge states of the lattice were obtained numerically in a finite system. We also compare the expression of Berry curvatures in two- and three-band models. Finally, some non-symmorphic symmetries of the model are also examined briefly as in [1].

Key words: Topological insulators, edge state, spin-orbit coupling, Chern number, non-symmorphic symmetry

Acknowledgement

Contents

Part I

Introduction and background

Chapter 1

Introduction

1.1 Historical Overview

In the southeast center of Uppsala there is a small forest alongside a wide road. On the other side of the forest, facing the Uppsala Science Park and Polacksbacken where I worked on this thesis, is a large magnificent building that conveys history. This building, named after two famous Swedish physicists at Uppsala University, Anders Jonas Ångström and his son Knut Ångström, is the Platonic Academy ('Ακαδημια) of condensed matter physics in Sweden. This thesis is mainly influenced by Dr. Anders Jonas Ångström, who is most known as a co-founder of the optical spectroscopy which is used to discover the microscopic energy structure of condensed materials. It is no longer possible, like Anders Jonas or Knut Ångström, to be a master of the whole wide area of physics. But when it comes to the bottom line of physics, everything becomes the same: knowing how nature works. I myself as a prospective theoretical physics worker, will use own tools to play around in studying materials: quantum field theory in condensed matter physics.

One of the most important topics in condensed matter physics is to study the phases of matters or materials. In statistical mechanics, one often classically study the phase transition of ideal gases or ferromagnetism using Landau's method with respect to spontaneous symmetry breaking. But during the past few decades, the research on quantum Hall effects has entered into a new era where the notion of topological order is frequently emphasised [2] [3]. The quantum Hall state defines a topological phase of which the certain fundamental properties are not sensitive to the smooth changes in the parameters of materials and will remain invariant if the whole system does not undergo a quantum phase transition.

During the past few years, physicists from the field of condensed matter has discovered that the spin orbit coupling could lead to exotic topological insulating phases [4][5][6][7][8], which also were predicted and observed in real materials[9][10][11] [12][13][14]. It is known to us now that a topological insulator, like the conventional

insulator, has a bulk energy gap which separates the occupied conductance band from the empty valence band. In the two dimensional case, the edge of a topological insulator necessarily has gapless states which are protected by time-reversal symmetry. The topological insulator is related to the two dimensional integer quantum Hall effect which induces exotic edge states. Also, the edge states (or surface states in the three dimensional case) result in a conducting state that is unique and is different from conventional low-dimensional electronic systems. Besides these fundamental theories, the edge states could also be useful for the applications such as quantum computing and hardware storage in the future.

Although the concept of topological order could be elaborated with respect the to intricately correlated fractional quantum Hall effects using many-body approaches [15][16]which led to the 1998 Nobel Prize in Physics by Laughlin, Stormer and Tsui, topological considerations still apply to the simpler integer quantum Hall states [2] using single particle quantum mechanics. Under such circumstances, topological insulators are very similar to integer quantum Hall systems, and they can also be understood within the framework of band theory [17] from solid state physics.

1.2   The object: $\frac{1}{5}$-depleted square lattice

In this thesis, we are planning to study the band theory in the $\frac{1}{5}$-depleted square lattice, consisting of coupled plaquette unit cells, shown in Fig. 4.1a with two different nearest neighbor hoppings t_1 and t_2, representing the plaquette band and dimer band hopping respectively. In the $\frac{1}{5}$−depleted square lattice, one out of every five atoms have been removed. It was first discovered in the study of spin-gap calcium vanadate material. In most cases know so far, the Dirac-cone system seems to commonly found in the nearest-neighbor tight binding models on regularly depleted square lattices. The honeycomb[18] and Kagomé[19] lattices are examples of such systems, which can be regarded as the $\frac{1}{3}$- and $\frac{1}{4}$-depleted triangular lattices respectively. Also, these models were used in studies of metal-insulator phase transitions[20][21].

From Fig. 4.1a, we may infer that the original point-group symmetry of this lattice is C_4, though, as long as the nearest-neighbor hoppings are concerned; one can deform the lattice into the square lattice of diamonds shown in Fig. 4.1b. Thus, the point-group symmetry is enlarged into C_{4v}, which enables us to study the band theory with higher degrees of symmetry.

1.3   Models and methods

We will essentially deal with different kinds of tight binding models as well as analysing band structures of the $\frac{1}{5}$-depleted square lattice in the thesis. The fundamental methods we used here will be quantum mechanics, statistical physics and
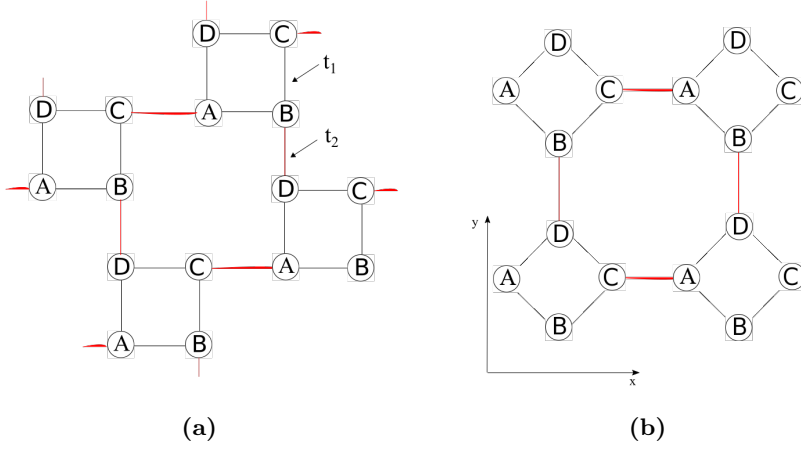
Figure 1.1: (a) The $\frac{1}{5}$-depleted square lattice where t_1 is the intrasquare and t_2 is the intersquare hopping. (b) Deformed $\frac{1}{5}$-depleted square lattice with C_{4v} symmetry.

condensed matter field theory. In Chapter 2, we will introduce the tight binding models, time-reversal symmetry and basic principles of spin-orbit coupling. In Chapter 3, much of the emphasis will be focused on the introduction of two dimensional topological insulator, which is a popular and contemporary topic in modern condensed matter physics. The three dimensional case for topological crystalline insulators and non-symmorphic symmetry effects on lattices and band structures will also be discussed briefly. Chapter 4 to 6 contains the main results of this thesis. We extend the results obtained by Yamashita in [22] and Chapter 4 mainly will deal with the effects of spin-orbit coupling on the band structure of the $\frac{1}{5}$-depleted square lattice, including both intrinsic and Rashba spin-orbit coupling. In Chapter 5, we prove that the $\frac{1}{5}$-depleted square lattice is a topological insulator using Berry curvature and the calculation of the spin Chern number. We also obtained the edge state of the lattice numerically. The effects of non-symmorphic symmetry on the lattice and band theory will be discussed in Chapter 6. And finally, the conclusion is drawn in Chapter 7.

Chapter 2

Tight-binding models and spin-orbit coupling

2.1   Introduction

In this chapter, we will introduce the core models which we use in the thesis, the tight-binding models together with the concept of spin-orbit coupling. Many of the derivations, ideas and formalism come from two useful references: most chapters in [23] by Shen and Chapter 1 and Chapter 2 in [24] by Altland & Simons. We first briefly introduce Bloch's theorem and band theory in Chapter 2.2. In Chapter 2.3 and 2.4 we will discuss second quantisation and the tight-binding models in the context of quantum field theory. Finally, in Chapter 2.5, spin-orbit coupling together with time-reversal symmetry will be discussed. Please note that this chapter may not contain everything in detail (Otherwise I will write a book on it, which I am not able to do right now.). Thus we only include topics which are closely related to my research shown in the following chapters.

2.2   The Bloch's theorem and band theory

The following illustrations were basically inspired by Chapter 4 from [23]. For detailed derivations readers may refer to [25] for elaborated ideas and concepts.

   A Bloch wave, also called a Bloch state, named after Swiss physicist Felix Bloch, is the wave function of an electron in a periodic potential. We now consider a Hamiltonian $\hat{\mathcal{H}}(\mathbf{r}) = \hat{\mathcal{H}}(\mathbf{r} + \mathbf{R})$ in a periodic potential. The eigenstates are of the following form:

$$|\psi_{n\mathbf{k}}(\mathbf{r})\rangle = \mathrm{e}^{\mathrm{i}\mathbf{k}\cdot\mathbf{r}}|u_{n\mathbf{k}}(\mathbf{r})\rangle \tag{2.1}$$

where $u_{n\mathbf{k}}(\mathbf{r})$ has the period of the crystal lattice $\mathbf{R}$ with $u_{n\mathbf{k}}(\mathbf{r}) = u_{n\mathbf{k}}(\mathbf{r} + \mathbf{R})$. Also, $u_{n\mathbf{k}}(\mathbf{r})$ is the periodic eigenstate of $H(\mathbf{k}) = \mathrm{e}^{-\mathbf{ik}\cdot\mathbf{r}}\mathcal{H}(\mathbf{r})\mathrm{e}^{\mathbf{ik}\cdot\mathbf{r}}$, which satisfies,

$$H(\mathbf{k})|\psi_{n\mathbf{k}}(\mathbf{r})\rangle = E_{n,\mathbf{k}}|\psi_{n\mathbf{k}}(\mathbf{r})\rangle \tag{2.2}$$

The energy of the eigenvalue satisfy that $E_{n,\mathbf{k}} = E_{n,\mathbf{k}+\mathbf{K}}$, which is periodic with periodicity $\mathbf{K}$ of a reciprocal lattice vector. The energies associated with the index n vary continuously with the wave vector $\mathbf{k}$ and form an energy band identified by the band index n. The eigenvalues for a given n are periodic in $\mathbf{k}$; all distinct values of $E_n(\mathbf{k})$ are located within the first Brillouin zone of the reciprocal lattice.

As is known to all, when an external field is applied to a material, it will force electrons to shift away from the equilibrium position, and then obtain a nonzero total momentum to form a flow of electric current. If the band is fully filled, and there exists an energy gap between the filled valence band and the unfilled conduction band, then this is called a band insulator. Much of our work in this thesis will be focused on the band structure and band theory. The study on the band theory is a very important research field in physics which lasted for decades. Now the notion of topology has also been introduced into this field, making the topological classification of the band structure possible for us.

2.3   Second quantization

Second quantization is a technique used in quantum field theory with accordance to the motivation of dealing with indistinguishable particles. The explicit symmetrisation of the wavefuncions is necessitated by quantum mechanical indistinguishability, since for fermions the wave function has to be anti-symmetric, while for bosons the wave function has to be symmetric. Thus, the symmetric or anti-symmetric representation might be very useful for physicists.

We consider two indistinguishable particles: particle one in state ψ_1 and particle two in state ψ_2. We have the following wavefunction:

$$\Psi(r_1, r_2) = \psi_1(r_1)\psi_2(r_2) \tag{2.3}$$

Then we will get the statement:

$$\Psi(r_1, r_2) = \pm\Psi(r_2, r_1) \tag{2.4}$$

$$\Psi(r_1, r_2) = \psi_1(r_1)\psi_2(r_2) \pm \psi_2(r_1)\psi_1(r_2) \tag{2.5}$$

where the $+$ sign is for bosons, and $-$ signs for fermions.

For n indistinguishable particles, we will have the wavefunction as:

$$\Psi(r_1, r_2, ..., r_n) = \sum_{\mathcal{P}} (\pm 1)^{\mathcal{P}} \psi_{i_1}(r_1)\psi_{i_2}(r_2)...\psi_{i_n}(r_n) \tag{2.6}$$

where $\mathcal{P}$ is all permutation combinations, and there are $n!$ terms here. Here, we define $\mathcal{P} = 0$ for even permutations and $\mathcal{P} = 1$ for odd permutations. If n is large, the wavefunction will have a very complicated form of expression.

The problem arose in early 20th century when physicists realized that Schrödinger equations and wave functions are designed for distinguishable particles and people need to symmetrise or anti-symmetrise all the wavefunctions by hand. Thus, the Fock space is introduced where many-body quantum states are written in terms of occupation number basis or particle number basis:

$$|\Psi\rangle = |n_1, n_2, ..., n_N\rangle \tag{2.7}$$

where n_i is the number of particles in state $|\psi_i\rangle$. This method makes the particles indistinguishable automatically.

In Fock space, operators can be written in terms of creation and annihilation operators.

For fermions, if $c_i^\dagger$ and c_i represent the create or annihilate one particle in state i, and $|0\rangle$, $|1\rangle$ represent either there is no or one particle in state i, then:

$$c_i^\dagger|1\rangle = 0$$
$$c_i^\dagger|0\rangle = |1\rangle$$
$$c_i|1\rangle = |0\rangle$$
$$c_i|0\rangle = 0 \tag{2.8}$$

The fermion satisfies the anti-commutation law which is:

$$\{c_i, c_j\} = \{c_i^\dagger, c_j^\dagger\} = 0, \quad \{c_i, c_j^\dagger\} = \delta_{ij} \tag{2.9}$$

where the curly brackets is the anticommutator defined via:

$$\{A, B\} = AB + BA \tag{2.10}$$

Similarly, for bosons, we have:

$$b_i^\dagger|n_1, n_2, ..., n_N\rangle = \sqrt{n_i + 1}|n_1, n_2, ..., n_i + 1, n_N\rangle$$
$$b_i|n_1, n_2, ..., n_N\rangle = \sqrt{n_i}|n_1, n_2, ..., n_i - 1, n_N\rangle \tag{2.11}$$

where $b_i^\dagger$ and b_i mean that either create or annihilate one particle on state i.

The boson creation and annihilation operators satisfy the algebra:

$$[b_i, b_j] = [b_i^\dagger, b_j^\dagger] = 0 \quad [b_i, b_j^\dagger] = \delta_{ij} \tag{2.12}$$

2.4 Tight-binding models

Now we will move on to consider tight-binding models, which is one of the most important applications of second quantisation in condensed matter quantum field theory. In fact, there are many ways of deriving the tight-binding models. We here adopted the one used in [24]. Most of the mathematical details are neglected. One may refer to [25] for more details.

We will start from a single Hamiltonian for a non-interacting system as follows:

$$\hat{\mathcal{H}}_0 = \int d^d r a_\sigma^\dagger(\mathbf{r}) \left[\frac{\hat{\mathbf{p}}^2}{2m} + \mathrm{V}(\mathbf{r}) \right] a_\sigma(\mathbf{r}) \qquad (2.13)$$

What we mainly will do is to simplify Eq. (2.13). Let us first consider a "rarefied" lattice where the constituent ion cores are separated by a distance in excess of the typical Bohr radius of the valence band electrons. In this "atomic limit", the weight of the electron wavefunctions is "tightly bound" to the lattice centers. Here, in order to formulate a microscopic theory of interactions, it is trivial to expand the Hamiltonian in a local basis which reflects the atomic orbital states of the isolated ions. Such a representation is presented by the basis of so-called Wannier states, which are defined by:

$$|\psi_{\mathbf{R}n}\rangle = \frac{1}{\sqrt{N}} \sum_{\mathbf{k}}^{B.Z.} e^{-i\mathbf{k}\cdot\mathbf{R}} |\psi_{\mathbf{k}n}\rangle, \quad |\psi_{\mathbf{k}n}\rangle = \frac{1}{\sqrt{N}} \sum_{\mathbf{R}}^{B.Z.} e^{i\mathbf{k}\cdot\mathbf{R}} |\psi_{\mathbf{R}n}\rangle, \qquad (2.14)$$

where $n = 1, 2, ..., N$, and $\mathbf{R}$ is the coordinates of the lattice centres, and $\sum_{\mathbf{k}}^{B.Z.}$ represents a summation over all momenta $\mathbf{k}$ in the first Brillouin zone. The Wannier function is thus defined as:

$$\psi_{\mathbf{R}n} = \langle \mathbf{r}|\psi_{\mathbf{R}n}\rangle \qquad (2.15)$$

The next major question to consider is how can the Wannier basis be used to obtain a simplified representation of the general Hamiltonian. We notice here that the Wannier states $\{|\psi_{\mathbf{R}n}\rangle\}$ will form an orthonormal basis for the Hilbert space. This means that the transformation between the real space and the Wannier representation is unitary,

$$|\mathbf{r}\rangle = \sum_{\mathbf{R}} |\psi_{\mathbf{R}}\rangle\langle\psi_{\mathbf{R}}|\mathbf{r}\rangle = \sum_{\mathbf{R}} \psi_{\mathbf{R}}^*(\mathbf{r})|\psi_{\mathbf{R}}\rangle \qquad (2.16)$$

In such case, we can get a relationship between the real space and the Wannier space operator basis as follows:

$$a_\sigma^\dagger(\mathbf{r}) = \sum_{\mathbf{R}} \psi_{\mathbf{R}}^*(\mathbf{r}) a_{\mathbf{R}\sigma}^\dagger = \sum_{i} \psi_{\mathbf{R}i}^*(\mathbf{r}) a_{i\sigma}^\dagger \qquad (2.17)$$

Note that in the second representation listed above, we have labeled the lattice centre coordinates $\mathbf{R} = \mathbf{R}_i$ by setting the index $i = 1, ..., N$. Then the unitary transformation between Bloch and Wannier states from Eq. (2.14) leads to an operator transformation

$$a_{\mathbf{k}\sigma}^\dagger = \frac{1}{\sqrt{N}} \sum_{i} e^{i\mathbf{k}\cdot\mathbf{R}_i} a_{i\sigma}^\dagger, \quad a_{i\sigma}^\dagger = \frac{1}{\sqrt{N}} \sum_{\mathbf{k}}^{B.Z.} e^{-i\mathbf{k}\cdot\mathbf{R}_i} a_{\mathbf{k}\sigma}^\dagger \qquad (2.18)$$

We could use Eq. (2.17) and Eq. (2.18) to formulate a Wannier representation of the Hamiltonian (2.13). Since the Bloch states are able to diagonalise the single-particle component $\hat{\mathcal{H}}_0$, we will get:

$$
\begin{aligned}
\hat{\mathcal{H}}_0 &= \sum_{\mathbf{k}} \epsilon_{\mathbf{k}} a_{\mathbf{k}\sigma}^\dagger a_{\mathbf{k}\sigma} \\
&= \frac{1}{N} \sum_{ii'} \sum_{\mathbf{k}} e^{i\mathbf{k}(\mathbf{R}_i - \mathbf{R}_{i'})} \epsilon_{\mathbf{k}} a_{i\sigma}^\dagger a_{i'\sigma} \\
&= \sum_{ii'} a_{i\sigma}^\dagger t_{ii'} a_{i'\sigma}
\end{aligned}
\tag{2.19}
$$

where we defined:

$$
t_{ii'} = \frac{1}{N} \sum_{\mathbf{k}} e^{i\mathbf{k}(\mathbf{R}_i - \mathbf{R}_{i'})} \epsilon_{\mathbf{k}}
\tag{2.20}
$$

Thus, we see that the new representation of the general Hamiltonian explains the electrons hopping from one lattice center i' to another, i. The strength of the hopping matrix element $t_{ii'}$ is controlled by the effective overlap of neighboring atoms. The tight-binding models are useful in describing the physics in solid state physics with non-trivial hopping $t_{ii'}$.

2.5 Spin-orbit coupling and time-reversal symmetry

2.5.1 Spin-orbit coupling in $2D$ topological insulators

In the previous discussion, we ignored the spin degrees of freedom. In the real world, we have spin up and spin down electrons. Also, the spin motion and orbit motion are usually coupled together, and additional terms should therefore be appended to the Hamiltonian to describe this effect. If we consider free electrons moving in 2D (without the lattice), the Hamiltonian is:

$$
H = \sum_{\mathbf{k}} \begin{pmatrix} c_{\mathbf{k}\uparrow}^\dagger & c_{\mathbf{k}\downarrow}^\dagger \end{pmatrix} \mathcal{H} \begin{pmatrix} c_{\mathbf{k}\uparrow} \\ c_{\mathbf{k}\downarrow} \end{pmatrix}
\tag{2.21}
$$

Because the Hamiltonian is an Hermitian operator, $\mathcal{H}$ should be a Hermitian 2×2 matrix. Any Hermitian 2×2 matrix can be written in terms of identity and Pauli matrices:

$$
\mathcal{H} = \mathcal{H}_0 \mathbb{1} + \mathcal{H}_x \sigma_x + \mathcal{H}_y \sigma_y + \mathcal{H}_z \sigma_z
\tag{2.22}
$$

In general, the components of $\mathcal{H}_{x,y,z}$ shall be smooth functions on real space, and can be non-zero, so spin will be playing an important role in the kinetic energy.

The effect of spin-orbit coupling plays a major role in $2D$ topological insulators. We will take graphene as an example. There are two types of spin-orbit coupling in the case of graphene, which were illustrated in [4] known as Kane-Mele model. In this model, the complex hopping of the tight-binding models are spin-orbit coupling terms or spin-dependent hoppings. The first one is the intrinsic spin-orbit coupling:

$$\hat{\mathcal{H}}_{in} = \mathrm{i}\lambda \sum_{\langle\langle ij\rangle\rangle,\alpha\beta} c_{i\alpha}^{\dagger} \nu_{ij} \sigma_{\alpha\beta}^{z} c_{j\beta} \qquad (2.23)$$

where $\langle\langle ij\rangle\rangle$ sums up all the next-nearest neighbours in the lattice, and $\alpha\beta$ are indices for spins (either spin up or spin down, indicated as $\uparrow$ and $\downarrow$, respectively). ν_{ij} indicates the turning direction of the next-nearest neighbour hopping of electrons. This intrinsic term respects all of the symmetries of graphene.

The other one is the Rashba spin-orbit coupling of the form $(\mathbf{s} \times \mathbf{k}) \cdot \hat{z}$ which is a more realistic model:

$$\hat{\mathcal{H}}_{R} = \mathrm{i}\lambda_R \sum_{\langle ij\rangle\alpha\beta} c_{i\alpha}^{\dagger} \left(\sigma_{\alpha\beta} \times \mathbf{d}\right)_z c_{j\beta} \qquad (2.24)$$

This effect will be present in an anisotropic crystal, the interface between two materials, or the surface of a material. At the interface, because the two materials have different electron density, electron will redistribute near the interface, moving from one material to the other. This induces an electric field perpendicular to the interface. Here, the spin-orbit coupling strength λ_R is determined by the strength of the electric field. This term can open a gap in the band structure.

One may also understand spin-orbit coupling from an intuitive way. In general, the spin-orbit interaction can be written as:

$$\hat{\mathcal{H}} = t\hat{\mathrm{L}} \cdot \hat{\mathrm{S}} \qquad (2.25)$$

with $\hat{\mathrm{L}} = \hat{r} \times \hat{p}$, and t is just a constant with no dimension.

Consider an electron hopping to its next nearest neighbour on the honeycomb lattice. During its hop, the atom closest to it (not counting the atom it's hopping from or toward) has the coulomb potential which affects the hopping electron. You can use the right-hand rule to calculate the sign of this term (since $\hat{r}$ points towards the atom, $\hat{p}$ is the direction the electron is travelling, and $\hat{S}$ corresponds to spin-up or spin-down).

If you consider the electron hopping back along the same path, the momentum is now $-\hat{p}$, so the overall sign of $\hat{\mathcal{H}}$ will pick up a minus sign. This explains the antisymmetry of ν_{ij} in Eq. (2.23).

2.5.2   Time-reversal symmetry and Kramer's degeneracy

There are two major characteristics which could be derived from spin-orbit coupling from the perspective of quantum mechanics. We will describe them here briefly. One may refer to the book by J.J.Sakurai[26] for explicit details.

The time-reversal symmetry is represented by an anti-unitary operation, and as such it can always be written as the product $\mathcal{T} = \mathcal{U}\mathcal{K}$ of a unitary matrix $\mathcal{U}$ times the complex conjugation operators $\mathcal{K}$. Indeed a real Hamiltonian is a manifestation of time-reversal symmetry since $\mathcal{H} = \mathcal{H}^*$.

For systems with spin $1/2$, time-reversal symmetry is described by the operator:

$$\mathcal{T} = \mathrm{i}\sigma_y \mathcal{K}, \tag{2.26}$$

with σ_y the second Pauli matrix acting on the spin degree of freedom. In that case we have $\mathcal{T}^2 = -1$. A Hamiltonian with this type of time-reversal symmetry obeys the equation:

$$\mathcal{H} = \sigma_y \mathcal{H}^* \sigma_y. \tag{2.27}$$

We also know that the spin-orbit coupling would preserve the time-reversal symmetry $\mathcal{T}\sigma \to -\sigma$ and $\mathcal{T}\mathbf{k} \to -\mathbf{k}$. Then we have:

$$\mathcal{T}\sigma_i k_j^{2n+1} = (-\sigma_i)\,(-k_j)^{2n+1} = (-1)^{2n+2}\sigma_i k_j^{2n+1} = \sigma_i k_j^{2n+1} \tag{2.28}$$

Hamiltonians of this type have the following property: every energy eigenvalue E_n is doubly degenerate. This is the so-called *Kramers' degeneracy* in quantum mechanics.

Chapter 3

Topological insulators

In this chapter, we will give an overview of some of the essential properties of topological insulators as well as related properties of topology. We will also show an important example of a topological insulator, which has both been theoretically studied, graphene. This chapter does in no way try to give a complete description of topological insulators, neither is it intended to give detailed theoretical descriptions of why the phenomenas occur. The purpose is to give an introduction to some of the most important aspects, and to give a hint on the analogies and formalism, which will be used in later chapters.

3.1 Quantum spin Hall insulators and edge states

The insulating state is one of the most basic states of matter. According to band theory, a typical insulators usually has an energy gap, a conduction band and a valence band. Are *all* electrons states with an energy gap topologically equivalent to the vacuum (since we are talking about "topological" in this chapter)? The answer is no, and the counterexamples are fascinating states of matter.

A simple example is the integer quantum Hall state, which occurs when electrons confined to two dimensions are placed in a strong magnetic field. Unlike an ordinary band insulator, though, an electric field causes the cyclotron orbits to drift, leading to a Hall current characterized by the quantized Hall conductivity:

$$\sigma_{xy} = Ne^2/h \tag{3.1}$$

where N is the number of Landau levels.

Also, the quantised Landau levels with energy $\epsilon_m = \hbar\omega_c(m + 1/2)$ are induced by the quantisation of the electrons' circular orbits with cyclotron frequency ω_c. When N Landau levels are filled with the rest empty, an energy gap will separate the empty states and the occupied states similar to an insulator.

The 2D topological insulators are known as quantum spin Hall insulators. This state was originally theorized to exist in graphene and in 2D semiconductor systems with a uniform strain gradient. It was then predicted to exist, and was then observed, in HgCdTe quantum well structures. We hereby discuss a bit on quantum spin Hall effect using graphene as a model system.

Graphene is consist of carbon atoms arranged in hexagonal structure, as shown in Fig. 3.1. The structure can be seen as a triangular lattice with a basis of two atoms per unit cell shown in Fig. 3.1b the Brilliouin zone.

(a)

(b)
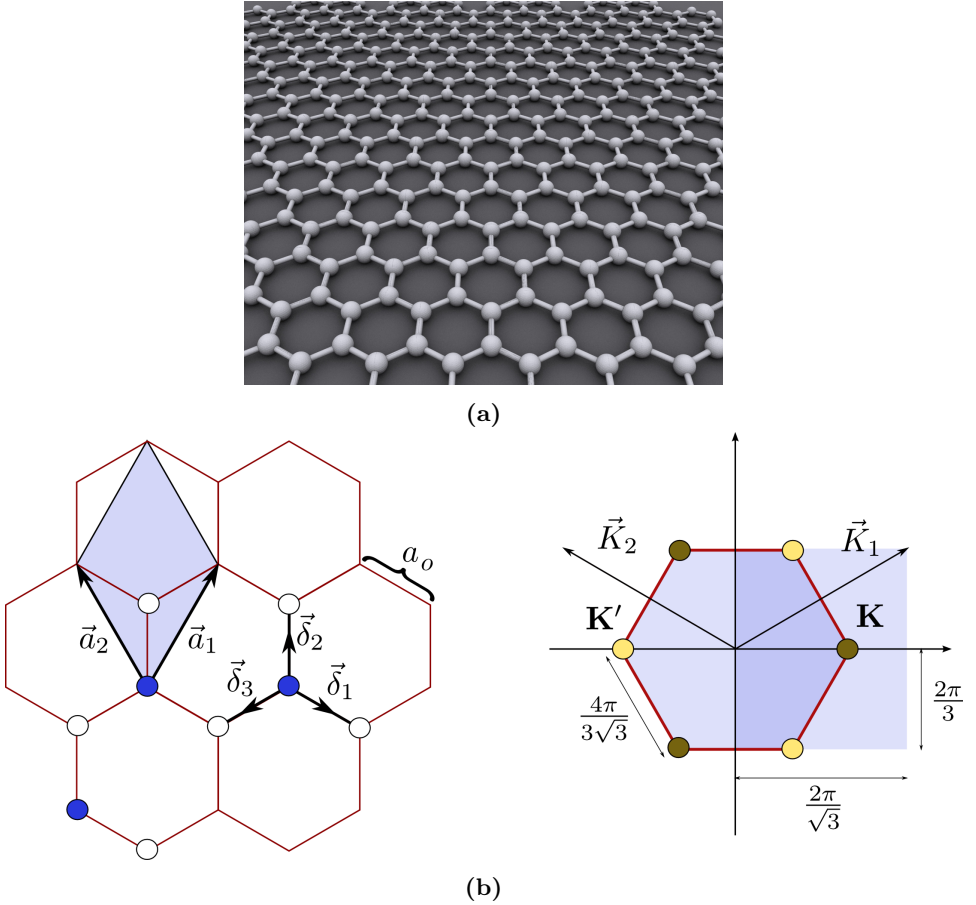
Figure 3.1: (a) Schematic of graphene material. (b). Honeycomb lattice and its Brillouin zone. (from [27])

The general Hamiltonian of this honeycomb lattice of graphene could be written as:

$$\hat{\mathcal{H}} = \mathbf{h}(\mathbf{k}) \cdot \vec{\sigma} \tag{3.2}$$

where $\mathbf{h}(\mathbf{k})$ is a smooth function in Brillouin zone, and $\vec{\sigma} = (\sigma_x, \sigma y, \sigma z)$ are Pauli matrices.

If we add the spin-orbit interaction into the graphene system, it will introduce a new mass term in Eq. (3.2) that respects all of symmetries of graphene. In the simplest picture, the intrinsic spin orbit interaction commutes with the electron spin S_z, so the Hamiltonian decouples into two independent Hamiltonians for the up and down spins. The resulting theory is simply two copies of the tight-binding model mentioned in Chapter 2 with opposite signs of the Hall conductivity for up and down spins. This does not violate $\mathcal{T}$ symmetry because time reversal flips both the spin and σ_{xy}. In an applied electric field, the up and down spins have Hall currents that flow in opposite directions. The Hall conductivity is thus zero, but there is a quantised spin Hall conductivity, defined by:

$$\mathrm{J}_x^{\uparrow} - \mathrm{J}_x^{\downarrow} = \sigma_{xy}^s E_y \tag{3.3}$$

with $\sigma_{xy}^s = e/2\pi$. This is the so-called quantum spin Hall effect.

The quantum spin Hall state must have gapless edge states since it is two copies of a quantum Hall state in Haldane model. Also, Kane and Mele (2005a) showed that the $\mathcal{T}$ will induce that the edge states in the quantum spin Hall insulators are robust even when spin conservation is violated because their crossing at $\mathbf{k} = 0$ is protected by the Kramers degeneracy, making the quantum spin Hall insulators a topological phase.

3.2 Topology and topological insulators

The idea of topology comes from geometry in the description of manifolds in three-dimensional space. Later, it was generalised to other dimensions and generic abstract spaces including the Hilbert space of quantum mechanics.

In geometry, if an manifold A could be adiabatically deformed into B, we say that they have the same topology, or they are topologically the same. In order to distinguish different manifolds, mathematician developed an object called topological index which is merely a number. For objects with the same topology, the index takes the same value. Otherwise they will be different. In the case of $2D$ closed manifold, the Euler characteristic provides an index:

$$\oiint_{\mathcal{M}} \mathrm{K}\, d\mathrm{S} = 2\pi \chi_{\mathcal{M}} \tag{3.4}$$

where the inverse radius gives the curvature $\mathrm{K} = 1/R$. Eq. (3.4) is called Gauss-Bonnet Theorem. $\chi_{\mathcal{M}}$ only deals with the topology of the manifold $\mathcal{M}$. In Fig. 3.2

(a) Sphere: $\chi_M = 2$

(b) Torus: $\chi_M = 0$

(c) Double torus: $\chi_M = -2$

(d) Triple torus: $\chi_M = -4$
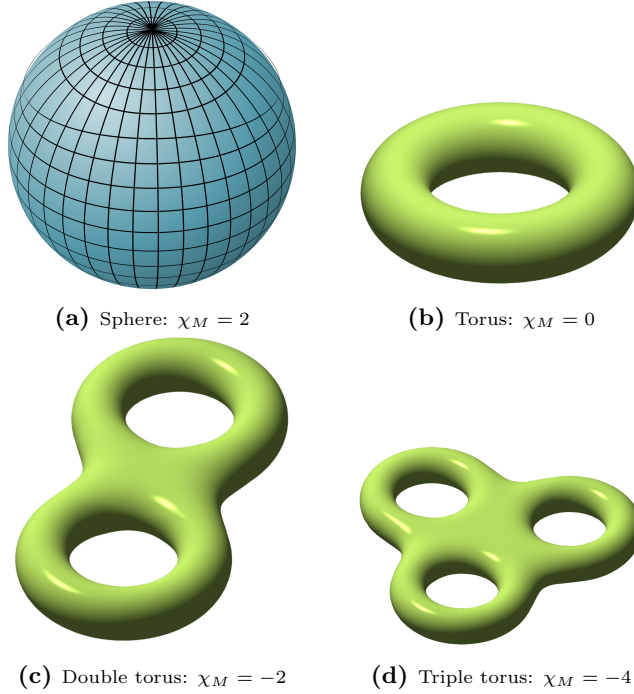
Figure 3.2: Topological index for different shapes (From wikipedia.org)

we show several different shapes with different topological index, which means that they can not be transformed into each other adiabatically.

Note that here we are considering closed manifolds without boundary. How is the topological index related to the band structure theory? The answer lies within the framework of bulk-boundary correspondence. A fundamental consequence of the topological classification of gapped band structures is the existence of gapless conducting states at interfaces where the topological invariant changes. The existence of such "one way" edge states is deeply related to the topology of the bulk quantum Hall state. Imagine an interface where a crystal slowly interpolates as a function of distance y between a quantum Hall state and a trivial insulator. One may wish that there exists a certain topological index which could distinguish between these two different materials. We find that somewhere along the way the energy gap has to vanish in quantum Hall insulator, because otherwise it is impossible for the topological invariant to change. There will therefore be low energy electronic states bound to the region where the energy gap passes through zero. Similar to Eq. (3.4), one may also introduce a certain index which is the integration of some curvature defined in Brillouin zone. The index is called "Chern number" named after Shiing-Shen Chern. Then it is possible to explicitly calculate

the edge states using a semi-infinite geometry with only one edge at $y = 0$.

The next question would be how to define Chern number, and what is its physical interpretation? We will come back to this in the next section.

3.3 Berry curvature and the Chern number

3.3.1 Berry connection

A key role in topological band theory is played by the Berry phase. The Berry phase arises because of the intrinsic phase ambiguity of a quantum mechanical wavefunction. The Bloch states are invariant under the transformation:

$$|u(\mathbf{k})\rangle \rightarrow e^{i\phi(\mathbf{k})}|u(\mathbf{k})\rangle \tag{3.5}$$

The transformation above is reminiscent of an electromagnetic gauge transformation, and thus we could come up with the definition of the Berry connection as:

$$\mathscr{A}_n = -i\langle u_{n,k}|\nabla_{\mathbf{k}}|u_{n,k}\rangle \tag{3.6}$$

where $\mathscr{A}_n$ is the Berry connection which is similar to the electromagnetic vector potential.

3.3.2 Berry curvature

We know that the vector potential is not a physical observable, and its value depends on the gauge choice. The quantity with physical meaning is the curl of it, which is the magnetic field B. Here, this generalises to the Berry curvature that is constructed from the Berry connection via the relation:

$$\begin{aligned}
\mathcal{F}_n = \nabla_k \times \mathscr{A}_n &= -i\epsilon_{ij}\partial_{k_i}\left\langle u_{n,k}\left|\partial_{k_j}\right|u_{n,k}\right\rangle \\
&= -i\epsilon_{ij}\left\langle\partial_{k_i}u_{n,k}|\partial_{k_j}u_{n,k}\right\rangle
\end{aligned} \tag{3.7}$$

3.3.3 Chern number in topological insulators

Now we can introduce the topological index, the Chern number as:

$$c = \frac{1}{2\pi}\sum_n \oiint_{B.Z.} \mathcal{F}\, d\mathbf{k} \tag{3.8}$$

where n is the index of bands. This index is defined as the integral over the occupied bands, the 2D Brillouin zone ($B.Z.$). Because a BZ has periodic boundary conditions along x and y, the $B.Z.$ is torus (since it is periodic, you can combine, for instance, the π/a and $-\pi/a$ along both x and y coordinates in $B.Z.$ and fold twice.) which is a closed manifold T^2.

The Chern number is also related to the Hall conductivity if we only count the valence bands ($n_{v.b.}$):

$$\sigma_{xy} = \frac{e^2}{h} \left[\frac{1}{2\pi} \sum_{n_{v.b.}} \oiint_{B.Z.} \mathcal{F} \, d\mathbf{k} \right] \tag{3.9}$$

For insulators, the Hall conductivity is a topological index and is an integer due to topological quantisation. In other words, the Berry curvature $\mathcal{F}$ induces the $2D$ topological insulators.

3.4   Non-symmorphic symmetry and band structure

In this thesis we consider a generalisation of the consideration of Kane and Young on this concept in Dirac semimetals [1].

It has long been known that non-symmorphic symmetries lead to extra degeneracies in electronic band structures that cause bands to remain degenerated because of the existence of higher dimensional projective representations of the little groups of certain values of $\mathbf{k}$ [28]. This fact can be understood as a simple consequence of fractional translation symmetries. Thus, non-symmorphic space groups are distinguished by the existence of symmetry operations which combine point group operations g with translations $\mathbf{t}$ that are a fraction of a Bravais lattice vector.

In the $2D$ case, the relevant operations for non-symmorphic symmetry is denoted as $\{g|\mathbf{t}\}$, are screw axes $g = C_{2\hat{\mathbf{n}}_\perp}$ ($\hat{\mathbf{n}}_\perp \perp \hat{z}$), glide mirror lines $g = M_{\hat{n}_\perp}$ and glide mirror planes $g = M_{\hat{z}}$, in connection with a half translation $\mathbf{t}$ that satisfies $g\mathbf{t} = \mathbf{t}$ and $e^{i\mathbf{G}\cdot\mathbf{t}} = -1$ for the odd reciprocal lattice vector $\mathbf{G}$. To sum up, a non-symmorphic symmetry $\{g|\mathbf{t}\}$ will protect degeneracies in the invariant line or plane in the Brillouin zone which satisfies $g\mathbf{k} = \mathbf{k}$. We will keep this principle in mind and look more into our $\frac{1}{5}$-depleted square lattice in the last part of the thesis.

Part II

Models and Results

Chapter 4

Effects of spin-orbit coupling

4.1   Introduction

The $\frac{1}{5}$-depleted square lattice[22] is depicted as follows in Fig. 4.1. We notice that there are four atoms per each primitive cell. We can label each cell with a pair of indices as (m, n) where m represents the index of x coordinate and n represents the index of y coordinate in real space, respectively.

| (a) | (b) |
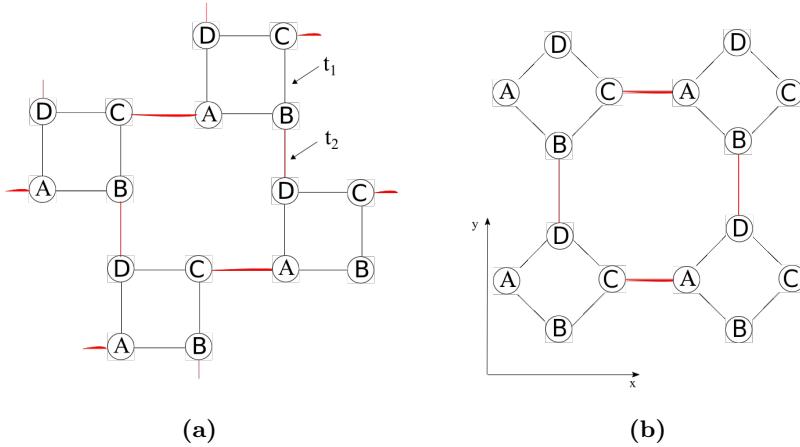
Figure 4.1: (a) The $\frac{1}{5}$-depleted square lattice where t_1 is the intrasquare and t_2 is the intersquare hopping. (b) Deformed $\frac{1}{5}$-depleted square lattice with C_{4v} symmetry.

The NN tight-binding model on the $\frac{1}{5}$-depleted square lattice is given by the expression: $\mathcal{H}^{(0)} = \sum_{\mathbf{k}\sigma} c^{\dagger}_{\mathbf{k}\alpha\sigma} H^{(0)\alpha\beta}_{\mathbf{k}\sigma} c_{\mathbf{k}\beta\sigma}$ with

$$
\hat{\mathcal{H}}^{(0)}_{\mathbf{k}\sigma} = \begin{pmatrix} 0 & t_1 & t_2 e^{-ik_x} & t_1 \\ t_1 & 0 & t_1 & t_2 e^{-ik_y} \\ t_2 e^{ik_x} & t_1 & 0 & t_1 \\ t_1 & t_2 e^{ik_y} & t_1 & 0 \end{pmatrix},
\tag{4.1}
$$

where $c^{\dagger}_{\mathbf{k}\alpha\sigma}$ creates a spin-up or down ($\sigma = \pm 1$) electrons at different positions of the sublattice indicated by $\alpha = A - D$. $\mathbf{k} = (k_x, k_y)$ is the momentum, and t_1 is the hopping constant within the primitive cell, and t_2 is the hopping constant between the nearest-neighbor primitive cells. Note that in this convention all atoms of one unit cell are moved onto the same position in real space. This does not affect the energy bands, only the wave functions.

We can thus solve the eigenvalue problem for the above Hamiltonian in (4.1), and obtain the band structure of the $\frac{1}{5}$-depleted square lattice as follows in Fig. 4.3. Also, the First Brillouin Zone is displayed in Fig. 4.2, where the corresponding high symmetry points and the direction of paths are indicated.
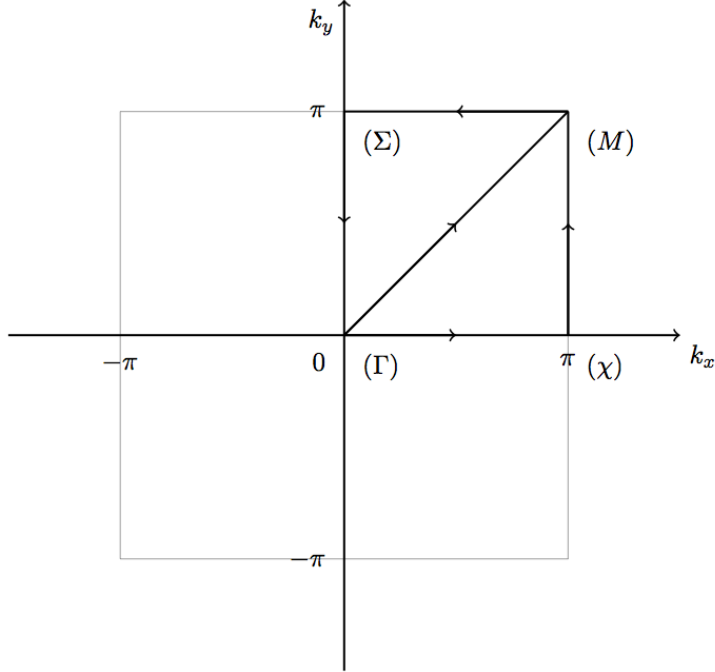
Figure 4.2: First Brillouin Zone of the $\frac{1}{5}$-depleted square lattice
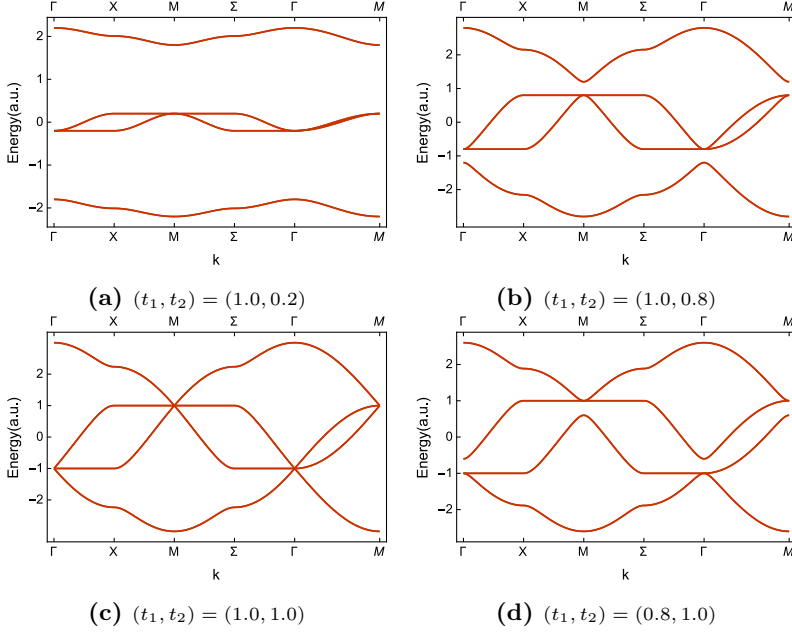
Figure 4.3: Dispersion relations for various (t_1, t_2) in $\frac{1}{5}$-depleted square lattice

Note that in Fig. 4.3c the parameters $(t_1, t_2) = (1.0, 1.0)$ give extra symmetry to the band structure as well as the "Dirac point" labeled as Γ in the figure.

4.2 Effects of the intrinsic SOC in band structure

4.2.1 Next-nearest neighbors

We can write down the intrinsic spin-orbit coupling Hamiltonian as [4]:

$$
\begin{aligned}
\hat{\mathcal{H}}_{in} &= i\lambda \sum_{\langle\langle ij, \alpha\beta\rangle\rangle} c_{i\alpha}^{\dagger} \nu_{ij} \sigma_{\alpha\beta}^{z} c_{j\beta} \\
&= i\lambda \sum_{\langle\langle ij\rangle\rangle} \nu_{ij} \begin{pmatrix} c_{i\uparrow}^{\dagger} & c_{i\downarrow}^{\dagger} \end{pmatrix} \begin{pmatrix} 1 & 0 \\ 0 & -1 \end{pmatrix} \begin{pmatrix} c_{j\uparrow} \\ c_{j\downarrow} \end{pmatrix} \\
&= i\lambda \sum_{\langle\langle ij\rangle\rangle} \nu_{ij} \begin{pmatrix} c_{i\uparrow}^{\dagger} & c_{i\downarrow}^{\dagger} \end{pmatrix} \begin{pmatrix} c_{j\uparrow} \\ -c_{j\downarrow} \end{pmatrix} \\
&= i\lambda \sum_{\langle\langle ij\rangle\rangle} \nu_{ij} \left(c_{i\uparrow}^{\dagger} c_{j\uparrow} - c_{i\downarrow}^{\dagger} c_{j\downarrow} \right),
\end{aligned}
\tag{4.2}
$$

where $\langle\langle ij \rangle\rangle$ sums up all the next-nearest neighbours in the lattice, and $\alpha\beta$ are indices for spins (either spin up or spin down, indicated as $\uparrow$ and $\downarrow$, respectively). The intrinsic spin-orbit coupling term is spin-dependent yet we could also write it in a coordinate independent form as $\mathrm{i}\,(\mathbf{d}_1 \times \mathbf{d}_2) \cdot \mathbf{s}$ where $\mathbf{d}_1$ and $\mathbf{d}_2$ are two vectors the electron travels from site j to site i. ν_{ij} indicates the turning direction of the next-nearest neighbour hopping of electrons. Here, we set $\nu_{ij} = +1$ for clockwise and $\nu_{ij} = -1$ for counter-clockwise. The next-nearest neighbour hopping and the directions for each hopping are depicted in Fig. 4.4:
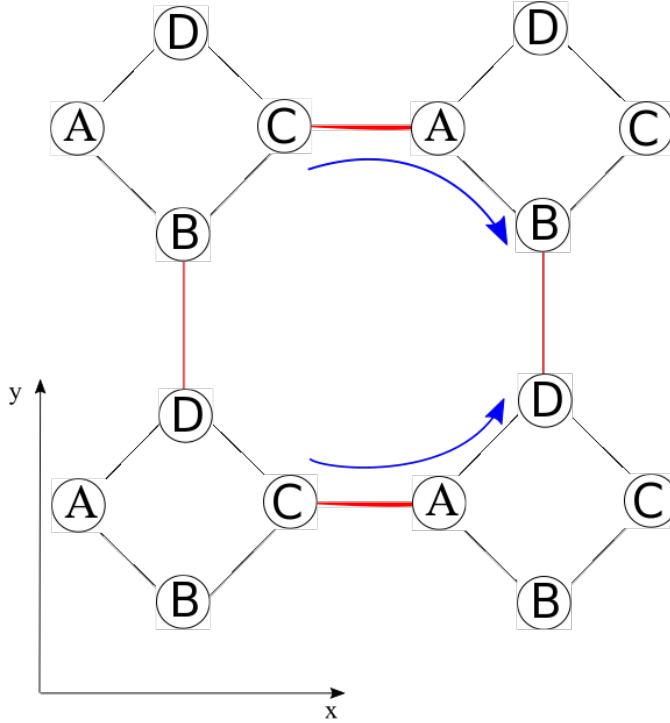
Figure 4.4: The next-nearest neighbour hopping of the $\frac{1}{5}$-depleted square lattice

We could also assume that the whole lattice is infinite in the two dimensional plane. Thus, one can introduce the Fourier decomposition of each operator in real

space into k space:

$$c_{m,n} = \frac{1}{\sqrt{N_s}} \int_{BZ} d\mathbf{k} \cdot c_{\mathbf{k}} e^{ik_x x_m} e^{ik_y y_n} \tag{4.3}$$

$$c_{m,n}^{\dagger} = \frac{1}{\sqrt{N_s}} \int_{BZ} d\mathbf{k} \cdot c_{\mathbf{k}}^{\dagger} e^{-ik_x x_m} e^{-ik_y y_n}, \tag{4.4}$$

where N_s is the normalisation constant. BZ and $\mathbf{k} = (k_x, k_y)$ indicates the integration over all Brillouin Zone.

For the intrinsic spin-orbit coupling situation, we obtained the next-nearest neighbour hopping terms on each site within one primitive cell (A, B, C, D). These expressions of creation and annihilation operators are essentially in the real space. The next step will be express all these terms in the momentum space by Fourier decomposition of each operator from Eq. (4.3) and (4.4).

We assume the whole lattice model is infinite in two dimension. The detailed calculations are elaborated here. We will take the $c_D^{m-1,n\dagger} \cdot c_A^{m,n}$ and $c_A^{m,n\dagger} \cdot c_D^{m-1,n}$ as two examples. Please note that after the Fourier decomposition we omit spin indices.

4.2.2 Fourier decomposition of the operators

First, we will take a look at the Fourier transformation relations of operators and elaborate the commutation relations. Here, we see that the real space is discrete and the momentum space is continuous with periodic boundary condition.

From Eq. (4.3) and Eq. (4.4), we will get the Fourier decomposition of the creation and annihilation operator, both seperately in the momentum space as :

$$c_{\mathbf{k}} = \frac{1}{\sqrt{N_s}} \sum_i c_i e^{-i\mathbf{k}x_i} \tag{4.5}$$

$$c_{\mathbf{k}}^{\dagger} = \frac{1}{\sqrt{N_s}} \sum_i c_i^{\dagger} e^{i\mathbf{k}x_i} \tag{4.6}$$

Then we can write down the anti-commutation relation of the creation and annihilation operator in the momentum space:

$$\{c_{\mathbf{k}}, c_{\mathbf{k}}^{\dagger}\} = \left\{ \frac{1}{\sqrt{N_s}} \sum_i c_i e^{-i\mathbf{k}x_i}, \frac{1}{\sqrt{N_s}} \sum_i c_i^{\dagger} e^{i\mathbf{k}'x_j} \right\}$$

$$= \sum_{i,j} \left\{ c_i, c_j^{\dagger} \right\} \frac{1}{N_s} e^{-i\mathbf{k}x_i} \cdot e^{i\mathbf{k}'x_j}$$

$$= \frac{1}{N_s} \sum_{i,j} \delta_{ij} e^{-i(\mathbf{k}-\mathbf{k}')x_i} = \frac{1}{N_s} \sum_i e^{-i(\mathbf{k}-\mathbf{k}')x_i}$$

$$= \left\{ \frac{1}{N_s} = \frac{a}{2\pi} \right\} = a\delta[(\mathbf{k}-\mathbf{k}')a] = \delta(\mathbf{k}-\mathbf{k}') \tag{4.7}$$

where a is the spacing distance in the real space.

4.2.3   The intrinsic spin-orbit coupling Hamiltonian

We now start to construct the intrinsic spin-orbit coupling Hamiltonian. The process, as mentioned before, is rather simple yet algebraically tedious. We would like to take the hopping pair between position A and D as indicated above in Fig. 4.4. The rest of the hoppings are essentially similar to this case.

First, we consider the hopping from position A to D, and then write down the Fourier decomposition of operators at these two positions. Since the system is in the bulk, the momentum space is infinite in both x and y directions:

$$c_D^{m-1,n\dagger} = \left(\frac{1}{\sqrt{N_s}}\right)^2 \int_{-\infty}^{+\infty} dk_x \int_{-\infty}^{+\infty} dk_y \cdot c_D^{\mathbf{k}\dagger} \mathrm{e}^{-ik_x x_{m-1}} \cdot \mathrm{e}^{-ik_y y_n} \tag{4.8}$$

$$c_A^{m,n\dagger} = \left(\frac{1}{\sqrt{N_s}}\right)^2 \int_{-\infty}^{+\infty} dk_x' \int_{-\infty}^{+\infty} dk_y' \cdot c_D^{\mathbf{k}'\dagger} \mathrm{e}^{ik_x' x_m} \cdot \mathrm{e}^{ik_y' y_n} \tag{4.9}$$

We sum up the same hopping in both x and y directions, which reads:

$$\sum_{m,n} c_D^{m-1,n\dagger} c_A^{m,n\dagger} = \frac{1}{N_s^2} \sum_{m,n} \int_{-\infty}^{+\infty} dk_x \int_{-\infty}^{+\infty} dk_x' \int_{-\infty}^{+\infty} dk_y \int_{-\infty}^{+\infty} dk_y' \cdot \left(c_D^{\mathbf{k}\dagger} c_A^{\mathbf{k}} \right)$$

$$\cdot \underbrace{\left(\mathrm{e}^{-ik_x x_{m-1}} \mathrm{e}^{ik_x' x_m} \right)}_{①} \cdot \underbrace{\left(\mathrm{e}^{-ik_y y_n} \mathrm{e}^{ik_y' y_n} \right)}_{②} \tag{4.10}$$

We then elaborate the expression in ① and ②.

For ①: Since

$$x_m = x_{m-1} + a, \tag{4.11}$$

where a is the distance spacing of both x and y directions. Plug Eq. (11) back to ①, we have, if we extract a $1/N_s$ from the prefactor:

$$\frac{1}{N_s} \sum_m \mathrm{e}^{-ik_x x_{m-1}} \cdot \mathrm{e}^{ik_x'(x_{m-1}+a)} = \frac{1}{N_s} \sum_m \mathrm{e}^{-i\left(k_x - k_x'\right)x_{m-1}} \cdot \mathrm{e}^{ik_x' a}$$

$$= \left\{ \frac{1}{N_s} = \frac{1}{2\pi} \right\} = \delta\left(k_x - k_x'\right) \cdot \mathrm{e}^{ik_x' a} \tag{4.12}$$

For ②:

Similarly, we will get

$$\frac{1}{N_s} \sum_n \mathrm{e}^{-ik_y y_n} \cdot \mathrm{e}^{ik_y' y_n} = \frac{1}{N_s} \sum_n \mathrm{e}^{-i\left(k_y - k_y'\right)\cdot y_n}$$

$$= \delta\left(k_y - k_y'\right) \tag{4.13}$$

Now we can rewrite Eq. (4.10) as follows:

$$\sum_{m,n} c_D^{m-1,n\dagger} c_A^{m,n\dagger} = \left(\int_{-\infty}^{+\infty} dk_x \int_{-\infty}^{+\infty} dk_x' \cdot \delta\left(k_x - k_x'\right) \cdot e^{ik_x' a} \right)$$

$$\cdot \left(\int_{-\infty}^{+\infty} dk_x' \int_{-\infty}^{+\infty} dk_y \cdot \delta\left(k_y - k_y'\right) \right) \cdot \left(c_D^{\mathbf{k}\dagger} c_A^{\mathbf{k}} \right)$$

$$= \int_{-\infty}^{+\infty} dk_x \int_{-\infty}^{+\infty} dk_y \cdot \left(c_D^{\mathbf{k}\dagger} c_A^{\mathbf{k}} \right) \cdot e^{ik_x a} \tag{4.14}$$

For simplicity, we could neglect the k in the equation and simply consider $c_D^\dagger c_A$ as the term in the momentum space. It is clear that after the Fourier decomposition the term $c_D^{m-1,n\dagger} c_A^{m,n}$ becomes $c_D^\dagger c_A \cdot e^{ik_x a}$. Similarly, we will have $c_A^{m,n\dagger} c_D^{m-1,n}$ which after Fourier decomposition becomes $c_A^\dagger c_D \cdot e^{-ik_x a}$.

We could now write down all the interaction terms of the intrinsic spin-orbit coupling as below:

$$A : \left(c_D^\dagger c_A \right) \cdot \left(e^{ik_x a} + e^{ik_y a} \right) - \left(c_B^\dagger c_A \right) \cdot \left(e^{ik_x a} + e^{-ik_y a} \right) \tag{4.15}$$

$$B : \left(c_A^\dagger c_B \right) \cdot \left(e^{-ik_x a} + e^{ik_y a} \right) - \left(c_C^\dagger c_B \right) \cdot \left(e^{ik_x a} + e^{ik_y a} \right) \tag{4.16}$$

$$C : \left(c_B^\dagger c_C \right) \cdot \left(e^{-ik_x a} + e^{-ik_y a} \right) - \left(c_D^\dagger c_C \right) \cdot \left(e^{-ik_x a} + e^{ik_y a} \right) \tag{4.17}$$

$$D : \left(c_C^\dagger c_D \right) \cdot \left(e^{ik_x a} + e^{-ik_y a} \right) - \left(c_A^\dagger c_D \right) \cdot \left(e^{-ik_x a} + e^{-ik_y a} \right) \tag{4.18}$$

We could set the lattice spacing $a = 1$, and then rewrite the Hamiltonian from (2) in matrix form. Since ν_{ij} only changes a sign, and the Pauli matrix $\sigma_{\alpha\beta}^z$ has only diagonal components, we could just consider the up-left 4×4 part of the whole 8×8 Hamiltonian matrix, shown as follows:

$$\hat{\mathcal{H}}_{in} = i \cdot$$

$$\begin{pmatrix} 0 & t_3\left(e^{-ik_x} + e^{ik_y}\right) & 0 & -t_3\left(e^{-ik_x} + e^{-ik_y}\right) \\ -t_3\left(e^{ik_x} + e^{-ik_y}\right) & 0 & t_3\left(e^{-ik_x} + e^{-ik_y}\right) & 0 \\ 0 & -t_3\left(e^{ik_x} + e^{ik_y}\right) & 0 & t_3\left(e^{ik_x} + e^{-ik_y}\right) \\ t_3\left(e^{ik_x} + e^{ik_y}\right) & 0 & -t_3\left(e^{-ik_x} + e^{ik_y}\right) & 0 \end{pmatrix}$$

$$\tag{4.19}$$

Add this intrinsic Hamiltonian into the original null Hamiltonian, we have the following total Hamiltonian:

$$\hat{\mathcal{H}} = \hat{\mathcal{H}}_{k\sigma}^{(0)} + \hat{\mathcal{H}}_{in} \tag{4.20}$$

Solving the eigenvalue problem for Eq. (4.20), we can obtain the energy spectrum of the whole system, plotted in Fig. 4.5. Note that we set the intrinsic

(a) $(t_1, t_2) = (1.0, 1.0)$ **(b)** $(t_1, t_2) = (1.0, 0.2)$

(c) $(t_1, t_2) = (1.0, 0.8)$ **(d)** $(t_1, t_2) = (0.8, 1.0)$
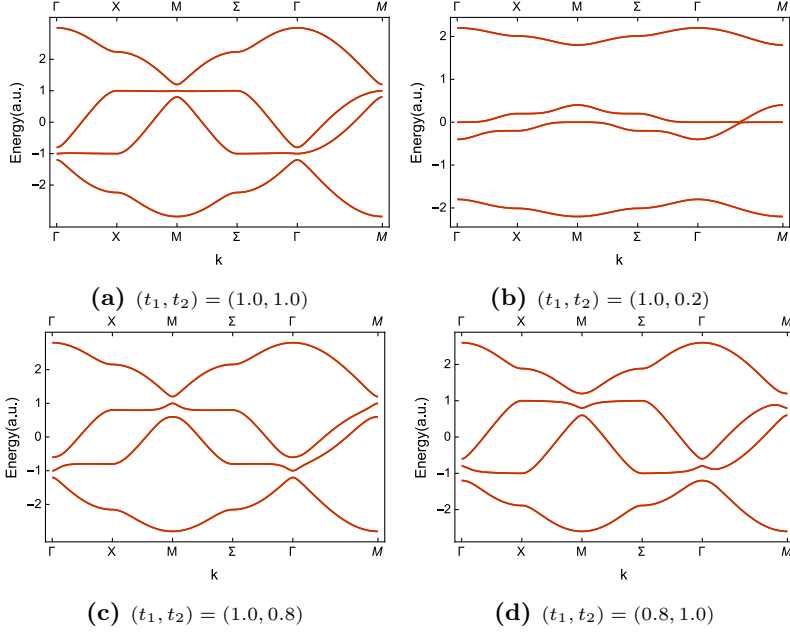
Figure 4.5: Dispersion relations for the entire system with the intrinsic spin-orbit coupling $t_3 = 0.1$

spin-orbit coupling factor $t_3 = 0.01$, which is two magnitude smaller than the hopping constants t_1 and t_2. From the results we could clearly witness that the gaps at the critical point is opened and the degeneracies are broken due to the additional the intrinsic spin-orbit coupling.

4.3   Effects of Rashba SOC on band structure

4.3.1   Rashba spin-orbit coupling Hamiltonian

From the previous discussion, we see that it was pretty much work to deal with the derivation of spin-orbit couplings. Fortunately, one could directly write down the term as hopping Hamiltonians as a tight-binding model, following the idea from Kane and Mele [4]. The Rashba spin-orbit coupling could also be done in the same way.

We first take a look at the Rashba spin-orbit coupling term. The illustration of the Rashba spin-orbit coupling hopping terms are depicted in Fig. 4.6:

$$\hat{\mathcal{H}}_R = i\lambda_R \sum_{\langle ij \rangle \alpha\beta} c_{i\alpha}^{\dagger} \left(\sigma_{\alpha\beta} \times \mathbf{d} \right)_z c_{j\beta} \tag{4.21}$$

where $\langle ij \rangle$ indicates at i and j are nearest-neighbor sites, and λ_R is the amplitude
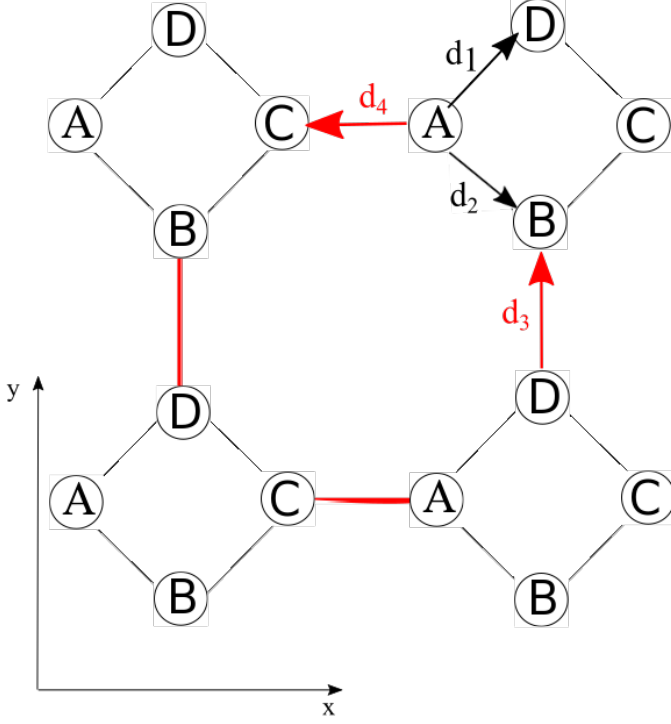
Figure 4.6: Illustration of the nearest-neighbor vectors d_i $(i = 1, 2, 3, 4)$ and different hoppings in $\frac{1}{5}$-depleted square lattice

of the Rashba SO coupling. The vector $\mathbf{d}$ refers to the direction of site i to the site j and corresponds to the nearest-neighbor vectors indicated in Fig. 4.6

From Fig. 4.6, we first take a look at the position A. Again we let all spacings b in the momentum space equal to a.

$$\hat{\mathcal{H}}_{R,A} = \mathrm{i}\lambda_R \sum_{\alpha\beta} \left[c_{A\alpha}^{m,n\dagger} \left(\sigma_{\alpha\beta} \times \mathbf{d}_1\right)_z c_{D\beta}^{m,n} + c_{A\alpha}^{m,n\dagger} \left(\sigma_{\alpha\beta} \times \mathbf{d}_2\right)_z c_{B\beta}^{m,n} \right.$$
$$\left. + c_{A\alpha}^{m,n\dagger} \left(\sigma_{\alpha\beta} \times \mathbf{d}_4\right)_z c_{C\beta}^{m-1,n} \right] \tag{4.22}$$

Note also that in the real space the coordinate of the vector **d** reads:

$$\mathbf{d}_1 = \left(\frac{\sqrt{2}}{2}, \frac{\sqrt{2}}{2} \right)$$

$$\mathbf{d}_2 = \left(\frac{\sqrt{2}}{2}, -\frac{\sqrt{2}}{2} \right)$$

$$\mathbf{d}_3 = (0, 1)$$

$$\mathbf{d}_4 = (-1, 0) \tag{4.23}$$

Plugging the Eq. (4.23) into Eq. (4.22), we have:

$$\hat{\mathcal{H}}_{R,A} = \mathrm{i}\lambda_R \sum_{\alpha\beta} \left[c_{A\alpha}^{m,n\dagger} \left(\sigma_x \cdot \frac{\sqrt{2}}{2} - \sigma_y \cdot \frac{\sqrt{2}}{2} \right) \cdot c_{D\beta}^{m,n} \right.$$

$$\left. + c_{A\alpha}^{m,n\dagger} \left(\sigma_x \cdot \left(-\frac{\sqrt{2}}{2} \right) - \sigma_y \cdot \frac{\sqrt{2}}{2} \right) \cdot c_{B\beta}^{m,n} + c_{A\alpha}^{m,n\dagger} \left(0 - \sigma_y \cdot (-1) \right) \cdot c_{C\beta}^{m-1,n} \right] \tag{4.24}$$

The Pauli matrices of σ_x and σ_y are:

$$\sigma_{\mathbf{x}} = \begin{pmatrix} 0 & 1 \\ 1 & 0 \end{pmatrix}, \sigma_{\mathbf{y}} = \begin{pmatrix} 0 & -\mathrm{i} \\ \mathrm{i} & 0 \end{pmatrix} \tag{4.25}$$

Using the expression from Eq. (4.8) we can then get:

$$\hat{\mathcal{H}}_{R,A} = \mathrm{i}\lambda_R \sum_{\alpha\beta} \left[c_{A\alpha}^{\dagger} \left(\begin{pmatrix} 0 & 1 \\ 1 & 0 \end{pmatrix} \cdot \frac{\sqrt{2}}{2} - \begin{pmatrix} 0 & -\mathrm{i} \\ \mathrm{i} & 0 \end{pmatrix} \cdot \frac{\sqrt{2}}{2} \right) c_{D\beta} \right.$$

$$+ c_{A\alpha}^{\dagger} \left(\begin{pmatrix} 0 & 1 \\ 1 & 0 \end{pmatrix} \cdot \frac{\sqrt{2}}{2} + \begin{pmatrix} 0 & -\mathrm{i} \\ \mathrm{i} & 0 \end{pmatrix} \cdot \frac{\sqrt{2}}{2} \right) c_{B\beta}$$

$$\left. + c_{A\alpha}^{\dagger} \begin{pmatrix} 0 & -\mathrm{i} \\ \mathrm{i} & 0 \end{pmatrix} c_{C\beta} \cdot \mathrm{e}^{-\mathrm{i}k_x} \right] \tag{4.26}$$

where we neglect the upper indices for each creation and annihilation operator indicating that they are in the momentum space. As what we previously did, we could simply expand the expression in terms of spins and write it explicitly as

follows:

$$\hat{\mathcal{H}}_{R,A} = \mathrm{i}\lambda_R \Bigg[\begin{pmatrix} c_{A\uparrow}^\dagger & c_{A\downarrow}^\dagger \end{pmatrix} \begin{pmatrix} 0 & \frac{\sqrt{2}}{2} + \frac{\sqrt{2}}{2}\mathrm{i} \\ \frac{\sqrt{2}}{2} - \frac{\sqrt{2}}{2}\mathrm{i} & 0 \end{pmatrix} \begin{pmatrix} c_{D\uparrow} \\ c_{D\downarrow} \end{pmatrix}$$

$$- \begin{pmatrix} c_{A\uparrow}^\dagger & c_{A\downarrow}^\dagger \end{pmatrix} \begin{pmatrix} 0 & \frac{\sqrt{2}}{2} - \frac{\sqrt{2}}{2}\mathrm{i} \\ \frac{\sqrt{2}}{2} + \frac{\sqrt{2}}{2}\mathrm{i} & 0 \end{pmatrix} \begin{pmatrix} c_{B\uparrow} \\ c_{B\downarrow} \end{pmatrix}$$

$$+ \begin{pmatrix} c_{A\uparrow}^\dagger & c_{A\downarrow}^\dagger \end{pmatrix} \begin{pmatrix} 0 & -\mathrm{i}\cdot\mathrm{e}^{-\mathrm{i}k_x} \\ \mathrm{i}\cdot\mathrm{e}^{-\mathrm{i}k_x} & 0 \end{pmatrix} \begin{pmatrix} c_{C\uparrow} \\ c_{C\downarrow} \end{pmatrix} \Bigg]$$

$$= \lambda_R \cdot \Bigg[\left(-\frac{\sqrt{2}}{2} + \frac{\sqrt{2}}{2}\mathrm{i} \right) c_{A\uparrow}^\dagger c_{D\downarrow} + \left(\frac{\sqrt{2}}{2} + \frac{\sqrt{2}}{2}\mathrm{i} \right) c_{A\downarrow}^\dagger c_{D\uparrow}$$

$$- \left(\frac{\sqrt{2}}{2} + \frac{\sqrt{2}}{2}\mathrm{i} \right) c_{A\uparrow}^\dagger c_{B\downarrow} - \left(-\frac{\sqrt{2}}{2} + \frac{\sqrt{2}}{2}\mathrm{i} \right) c_{A\downarrow}^\dagger c_{B\uparrow}$$

$$+ \mathrm{e}^{-\mathrm{i}k_x} c_{A\uparrow}^\dagger c_{C\downarrow} - \mathrm{e}^{-\mathrm{i}k_x} c_{A\downarrow}^\dagger c_{C\downarrow} \Bigg] \tag{4.27}$$

Note that the spin is no longer conserved so that we can not work within the 4×4 matrix and then we have to extend it to the 8×8 matrix later. Similarly, we can go through all four positions and write down the Rashba Hamiltonian as follows:

$$\hat{\mathcal{H}}_{R,B} = \lambda_R \cdot \Bigg[\left(\frac{\sqrt{2}}{2} + \frac{\sqrt{2}}{2}\mathrm{i} \right) c_{B\uparrow}^\dagger c_{A\downarrow} + \left(-\frac{\sqrt{2}}{2} + \frac{\sqrt{2}}{2}\mathrm{i} \right) c_{B\downarrow}^\dagger c_{A\uparrow}$$

$$+ \left(-\frac{\sqrt{2}}{2} + \frac{\sqrt{2}}{2}\mathrm{i} \right) c_{B\uparrow}^\dagger c_{C\downarrow} + \left(\frac{\sqrt{2}}{2} + \frac{\sqrt{2}}{2}\mathrm{i} \right) c_{B\downarrow}^\dagger c_{C\uparrow}$$

$$+ \left(-\mathrm{i}\cdot\mathrm{e}^{-\mathrm{i}k_y} \right) c_{B\uparrow}^\dagger c_{D\downarrow} + \left(-\mathrm{i}\cdot\mathrm{e}^{-\mathrm{i}k_y} \right) c_{B\downarrow}^\dagger c_{D\uparrow} \Bigg] \tag{4.28}$$

$$\hat{\mathcal{H}}_{R,C} = \lambda_R \cdot \Bigg[\left(\frac{\sqrt{2}}{2} - \frac{\sqrt{2}}{2}\mathrm{i} \right) c_{C\uparrow}^\dagger c_{B\downarrow} + \left(-\frac{\sqrt{2}}{2} - \frac{\sqrt{2}}{2}\mathrm{i} \right) c_{C\downarrow}^\dagger c_{B\uparrow}$$

$$+ \left(\frac{\sqrt{2}}{2} + \frac{\sqrt{2}}{2}\mathrm{i} \right) c_{C\uparrow}^\dagger c_{D\downarrow} + \left(-\frac{\sqrt{2}}{2} + \frac{\sqrt{2}}{2}\mathrm{i} \right) c_{C\downarrow}^\dagger c_{D\uparrow}$$

$$+ \left(\mathrm{e}^{\mathrm{i}k_x} \right) c_{C\uparrow}^\dagger c_{A\downarrow} + \left(\mathrm{e}^{\mathrm{i}k_x} \right) c_{C\downarrow}^\dagger c_{A\uparrow} \Bigg] \tag{4.29}$$

$$\hat{\mathcal{H}}_{R,D} = \lambda_R \cdot \Bigg[\left(\frac{\sqrt{2}}{2} - \frac{\sqrt{2}}{2}\mathrm{i} \right) c_{D\uparrow}^\dagger c_{A\downarrow} + \left(-\frac{\sqrt{2}}{2} - \frac{\sqrt{2}}{2}\mathrm{i} \right) c_{D\downarrow}^\dagger c_{A\uparrow}$$

$$+ \left(\mathrm{i} \cdot \mathrm{e}^{\mathrm{i}k_y} \right) c_{D\uparrow}^\dagger c_{B\downarrow} + \left(\mathrm{i} \cdot \mathrm{e}^{\mathrm{i}k_y} \right) c_{D\downarrow}^\dagger c_{B\uparrow}$$

$$+ \left(-\frac{\sqrt{2}}{2} - \frac{\sqrt{2}}{2}\mathrm{i} \right) c_{D\uparrow}^\dagger c_{C\downarrow} + \left(\frac{\sqrt{2}}{2} - \frac{\sqrt{2}}{2}\mathrm{i} \right) c_{D\downarrow}^\dagger c_{C\uparrow} \Bigg] \qquad (4.30)$$

4.3.2   Energy gaps induced by Rashba spin-orbit couplings

We then can plug all the above four equations into Eq. (4.21) and write it down in the matrix form, then append it with the null Hamiltonian from Eq. (4.1), we will get the Hamiltonian of the whole system with Rashba spin-orbit couplings:

$$\hat{\mathcal{H}} = \hat{\mathcal{H}}_k^{(0)} + \hat{\mathcal{H}}_R \qquad (4.31)$$

Note here the $\hat{\mathcal{H}}_k^{(0)}$ is a 8×8 matrix by simply copying the same block of the previous $\hat{\mathcal{H}}_{k\sigma}^{(0)}$ from Eq. (4.1). We then solve the eigenvalue problem of the (4.31) and then obtain the results of band structure as follows: We plot for the same Rashba SOC

(a) $(t_1, t_2, t_4) = (1.0, 0.2, 0.03)$ **(b)** $(t_1, t_2, t_4) = (1.0, 0.8, 0.03)$

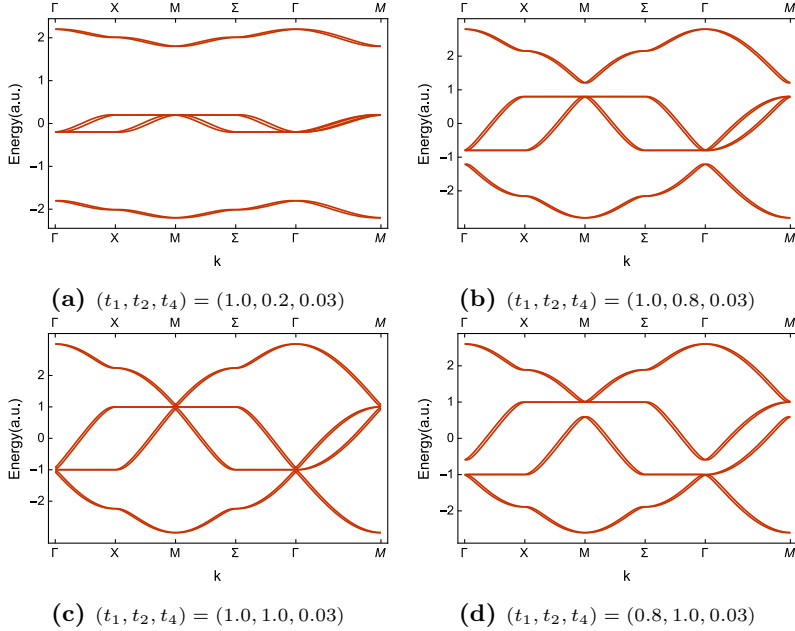**(c)** $(t_1, t_2, t_4) = (1.0, 1.0, 0.03)$ **(d)** $(t_1, t_2, t_4) = (0.8, 1.0, 0.03)$

Figure 4.7: Dispersion relations with the same strength of Rashba spin-orbit couplings

strength in Fig. 4.7. We compare this with the case without spin-orbit coupling in Fig. 4.3. We could also get them for different Rashba SOC strength as in Fig. 4.8.
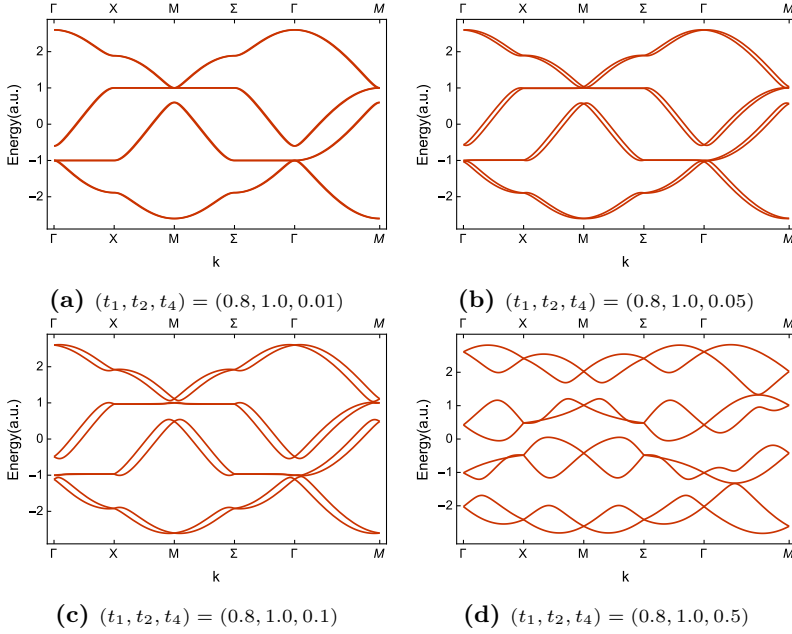
(a) $(t_1, t_2, t_4) = (0.8, 1.0, 0.01)$

(b) $(t_1, t_2, t_4) = (0.8, 1.0, 0.05)$

(c) $(t_1, t_2, t_4) = (0.8, 1.0, 0.1)$

(d) $(t_1, t_2, t_4) = (0.8, 1.0, 0.5)$

Figure 4.8: Dispersion relations with different strength of Rashba spin-orbit couplings

We now could have some comment on the effect of spin-orbit couplings on the band structure. Since the spin-orbit coupling will preserve the time-reversal symmetry, and time-reversal symmetry will lead to the Kramer's degeneracy, we find that around certain Dirac point and other time-reversal symmetric momenta like M, χ and Σ, for each eigenvalue of energy, there exists a two-fold degenerate state. This result is consistent with the theory of topological insulator with time-reversal symmetry.

We may also turn on both intrinsic and Rashba spin-orbit couplings to see how they will affect the band structure. They are plotted in Fig. 4.9 with $(t_1, t_2) = (0.8, 1.0)$ and in Fig. 4.10 with $(t_1, t_2) = (1.0, 1.0)$. By comparing the band structure patterns in these two figures, we find that the Rashba spin-orbit couplings will break down the degeneracies along the nodal lines between critical Dirac points in the Brillouin zone. We also find that the intrinsic and Rashba spin-orbit couplings will open up the energy gaps at certain critical momenta like Γ and M as well as leading to the band crossovers, where the intrinsic ones have large effects on opening the gap. This is due to the addition of the Rashba spin-orbit interaction terms. Before adding the spin-orbit couplings, the band structure is consist of several Dirac cones. After adding it into the Hamiltonian of the whole system, it causes the shift of bands in the $\pm k_x$ direction of the Brillouin Zone, which contributes to the band structures in Fig. 4.10, making it totally different from the graphene case.

(a) $(t_3, t_4) = (0.0, 0.0)$ **(b)** $(t_3, t_4) = (0.01, 0.0)$

(c) $(t_3, t_4) = (0.0, 0.1)$ **(d)** $(t_3, t_4) = (0.01, 0.1)$
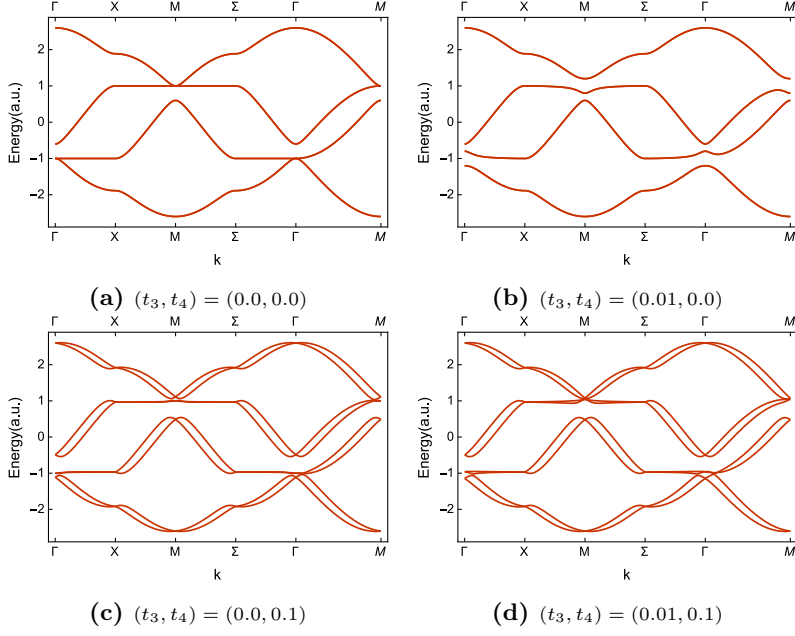
Figure 4.9: Dispersion relations with variously tuned Intrinsic and Rashba SOC where $(t_1, t_2) = (0.8, 1.0)$

(a) $(t_3, t_4) = (0.0, 0.0)$

(b) $(t_3, t_4) = (0.02, 0.0)$

(c) $(t_3, t_4) = (0.0, 0.1)$
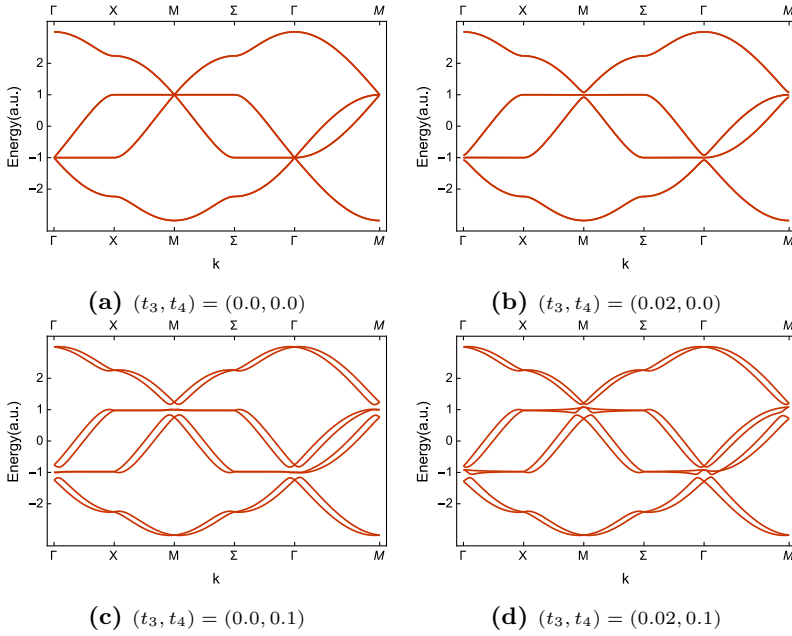
(d) $(t_3, t_4) = (0.02, 0.1)$

Figure 4.10: Dispersion relations with variously-tuned Intrinsic and Rashba SOC where $(t_1, t_2) = (1.0, 1.0)$

Chapter 5

Edge states

5.1 Introduction

In this chapter, we will focus on calculating the edge states of the $\frac{1}{5}$-depleted square lattice. Much of the calculation in this chapter is done from first principles. In Chapter 5.2, we will first introduce the $\mathbf{k} \cdot \mathbf{p}$, which is essentially the main method we used here to perturbatively obtain band structures of the lattice. We also briefly introduce the concepts of Gell-Mann matrices here, which are the $SU(3)$ operators and will be useful for the Dirac-like equation and its corresponding solution for edge states in Chapter 5.3. In Chapter 5.4, we will try to prove that the $\frac{1}{5}$-depleted square lattice is itself a topological insulator with respect to the Berry curvature and the elaboration of Chern number of the whole system where an important generalisation to the spin-1 representation of will be introduced in accordance with the Gell-mann matrices. We will compare the difference between both the two band and the three band model as well. In the last Chapter 5.5, we will numerically obtain the edge states of the $\frac{1}{5}$-depleted square lattice with intrinsic spin-orbit couplings using the recursion matrices, which are similar to the method used in graphene [18].

5.2 k · p method and Gell-Mann matrices

5.2.1 k · p method

The $\mathbf{k} \cdot \mathbf{p}$ method, or $\mathbf{k} \cdot \mathbf{p}$ theory which is usually pronounced as "k dot p", is an approximation scheme for calculating the band structure in solids. We hereby essentially follow the ideas and methods from [29] and check Chapter 2.8 if you are looking for detailed derivations.

In the $\mathbf{k} \cdot \mathbf{p}$ method, one is expected to obtain analytic expressions for band dispersion and effective masses around high-symmetry points. The $\mathbf{k} \cdot \mathbf{p}$ method can actually be derived from the one-electron Schrödinger equation. We could simply

use the Bloch theorem from Eq. (2.1) and rewrite it in the space representation, in the reduced zone scheme, as follows:

$$\psi_{n\mathbf{k}}\left(\mathbf{r}\right) = \mathrm{e}^{\mathrm{i}\mathbf{k}\cdot\mathbf{r}}u_{n\mathbf{k}}\left(\mathbf{r}\right), \tag{5.1}$$

When we insert the Eq. (5.1) into the one-electron Schrödinger equation with potential V, we will get the equation in $u_{n\mathbf{k}}$ of the form:

$$\left(\frac{p^2}{2m} + \frac{\hbar\mathbf{k}\cdot\mathbf{p}}{m} + \frac{\hbar^2 k^2}{2m} + V\right) u_{n\mathbf{k}+\mathbf{p}} = E_{n\mathbf{k}+\mathbf{p}}u_{n\mathbf{k}+\mathbf{p}} \tag{5.2}$$

When $\mathbf{k} = \mathbf{k}_0 = (0,0,0)$, Eq. (5.2) will be reduced to

$$\left(\frac{p^2}{2m} + V\right) u_{n\mathbf{p}} = E_{n\mathbf{p}}u_{n\mathbf{p}} \tag{5.3}$$

One can choose any critical or highly symmetric points other than $\mathbf{k}_0$ to do the similar things. Since the functions $u_{n\mathbf{0}}$ are periodic, it is much easier to solve Eq. (5.3) of which the solutions form a complete and orthonormal set of basis functions. Once we obtained the eigenfunctions ($u_{n\mathbf{p}}$) and eigenvalues ($E_{n\mathbf{p}}$), we can treat the terms $\frac{\hbar\mathbf{k}\cdot\mathbf{p}}{m}$ and $\frac{\hbar^2 k^2}{2m}$ as the additional perturbation terms using either degenerate or non degenerate perturbation theory from the formalism of quantum mechanics. This is the so-called $\mathbf{k}\cdot\mathbf{p}$ method. Note that since it is a perturbation theory, we expect that the value of $\mathbf{k}$ would be rather small within the range of the high symmetric point $\mathbf{k}_0$ while doing the expansion. In general, this method can be applied to calculate the band dispersion near any point $\mathbf{k}_0$ by expanding Eq. (5.2) around $\mathbf{k}_0$ provided the wave functions (or the matrix elements of $\mathbf{p}$ between these wave functions) and the energies at $\mathbf{k}_0$ are known. In our model and procedures shown below, we will only consider the first order term of expansion for necessity as it is enough for the results.

5.2.2   Gell-Mann matrices

After the discussion about the $\mathbf{k}\cdot\mathbf{p}$ method in the previous section, it is very essential for us to introduce the notion of Gell-Mann matrices here, which were named for Murray Gell-Mann. It is a representation of the infinitesimal generators of the special unitary group called $SU(3)$. One could generate the 3×3 matrices

Table 5.1: Non-zero structure constants f_{abc} of $SU(3)$

abc	123	147	156	246	257	345	367	458	678
f_{abc}	1	1/2	$-1/2$	1/2	1/2	1/2	$-1/2$	$\sqrt{3}/2$	$\sqrt{3}/2$

of $SU(3)$ from the Gell-Mann matrices as follows:

$$\lambda_1 = \begin{pmatrix} 0 & 1 & 0 \\ 1 & 0 & 0 \\ 0 & 0 & 0 \end{pmatrix} \qquad \lambda_2 = \begin{pmatrix} 0 & -\mathrm{i} & 0 \\ -\mathrm{i} & 0 & 0 \\ 0 & 0 & 0 \end{pmatrix} \qquad \lambda_3 = \begin{pmatrix} 1 & 0 & 0 \\ 0 & -1 & 0 \\ 0 & 0 & 0 \end{pmatrix} \tag{5.4}$$

$$\lambda_4 = \begin{pmatrix} 0 & 0 & 1 \\ 0 & 0 & 0 \\ 1 & 0 & 0 \end{pmatrix} \qquad \lambda_5 = \begin{pmatrix} 0 & 0 & -\mathrm{i} \\ 0 & 0 & 0 \\ \mathrm{i} & 0 & 0 \end{pmatrix} \qquad \lambda_6 = \begin{pmatrix} 0 & 0 & 0 \\ 0 & 0 & 1 \\ 0 & 1 & 0 \end{pmatrix}$$

$$\lambda_7 = \begin{pmatrix} 0 & 0 & 0 \\ 0 & 0 & -\mathrm{i} \\ 0 & \mathrm{i} & 0 \end{pmatrix} \qquad \lambda_8 = \frac{1}{\sqrt{3}} \begin{pmatrix} 1 & 0 & 0 \\ 0 & 1 & 0 \\ 0 & 0 & -2 \end{pmatrix}$$

The Gell-Mann matrices satisfy commutation relation,

$$[\lambda_a, \lambda_b] = 2\mathrm{i} f_{abc} \lambda_c \tag{5.5}$$

where $a, b, c = 1, 2, 3, ..., 8$, and where there is an implicit sum over c, and the structure constants f_{abc} are totally antisymmetric under the interchange of any pair of indices. The explicit form of the non-zero $SU(3)$ structure constants are listed in Table 1.

The Gell-Mann matrices and together with these important algebraic properties will essentially be used later when we are trying to calculate analytically the edge states of the $\frac{1}{5}$-depleted square lattice with spin-orbit couplings.

5.3   Dirac-like equation for edge states

We know the main idea of calculating the edge states is solving the eigenvalue problem of Hamiltonian as:

$$\hat{\mathcal{H}}\psi = E\psi \tag{5.6}$$

where E is the eigenvalue of the Hamiltonian $\hat{\mathcal{H}}$.

We hereby give out a perturbative method to solve this problem using $\mathbf{k} \cdot \mathbf{p}$ method. We will only consider the intrinsic spin-orbit couplings situation here for the calculation of edge states. From the results which we obtained in Chapter 4, we know that point $(k_x, k_y) = (0, 0)$ is a highly symmetric point for the perturbative expansion (See Fig. 4.5). We then take k_x, k_y as well as t_3, the strength for the intrinsic spin-orbit couplings as the small perturbation around $(k_x, k_y, t_3) = (0, 0, 0)$, the highly symmetric point.

We try to expand the whole Hamiltonian around this point as follows using multivariable Taylor expansion:

$$\hat{\mathcal{H}} = \hat{\mathcal{H}}_0 + k_x \cdot \partial_{k_x}\hat{\mathcal{H}}|_{k_x=0} + k_y \cdot \partial_{k_y}\hat{\mathcal{H}}|_{k_y=0} + t_3 \cdot \partial_{t_3}\hat{\mathcal{H}}|_{t_3=0} \qquad (5.7)$$

We find that Eq. (5.7) are in 4×4 matrices form. By analysing the eigenvalues of the total Hamiltonian at $(k_x, k_y, t_3) = (0, 0, t_3)$, where $(t_1, t_2) = (1.0, 1.0)$, we can find that the four eigenvalues of $\hat{\mathcal{H}}$ is:

$$\begin{aligned}
\Lambda_1 &= 3 \qquad\qquad\qquad\qquad\qquad\qquad (5.8)\\
\Lambda_2 &= -1\\
\Lambda_3 &= -1 + 8t_3\\
\Lambda_4 &= -1 - 8t_3
\end{aligned}$$

From Eq. (5.8), we noticed that apart from the largest one $\Lambda_1 = 3$ (we hereby use the capitalised Λ so that it is not confused with the Gell-Mann matrices), we have three eigenvalues which are near -1. We could then just realign the $\hat{\mathcal{H}}$ when $(t_1, t_2) = (1.0, 1.0)$, and then focus on the 3×3 block, where the additional one is only responsible for the hybridisation. W can write Eq. (5.7) into an explicit expression in a 3×3 form (the "block") as follows:

$$\begin{aligned}
\hat{\mathcal{H}} &= \begin{pmatrix} -1 & 0 & 0 \\ 0 & -1+8t_3 & 0 \\ 0 & 0 & -1-8t_3 \end{pmatrix} + k_x \cdot \begin{pmatrix} 0 & -\frac{1}{2} & \frac{1}{2} \\ -\frac{1}{2} & 0 & 0 \\ \frac{1}{2} & 0 & 0 \end{pmatrix} + k_y \cdot \begin{pmatrix} 0 & -\frac{i}{2} & \frac{i}{2} \\ -\frac{i}{2} & 0 & 0 \\ \frac{i}{2} & 0 & 0 \end{pmatrix}\\
&= -\mathbb{1} + t_3 \cdot \begin{pmatrix} 0 & 0 & 0 \\ 0 & 8 & 0 \\ 0 & 0 & -8 \end{pmatrix} + k_x \cdot \begin{pmatrix} 0 & -\frac{1}{2} & \frac{1}{2} \\ -\frac{1}{2} & 0 & 0 \\ \frac{1}{2} & 0 & 0 \end{pmatrix} + k_y \cdot \begin{pmatrix} 0 & -\frac{i}{2} & \frac{i}{2} \\ -\frac{i}{2} & 0 & 0 \\ \frac{i}{2} & 0 & 0 \end{pmatrix} \quad (5.9)
\end{aligned}$$

where $\mathbb{1}$ is the identity operator in three dimension.

The question now arose whether we could write Eq. (5.9) into Dirac-like equation as described in the two dimensional case [23] in order to analytically calculate the edge states of the system. The conventional method would be trying to diagonalise the Hamiltonian $\hat{\mathcal{H}}$ in some mutual basis of each block matrix. One possible way would be introducing a matrix and multiplied it and its inverses matrix on both sides of the Hamiltonian $\hat{\mathcal{H}}$. It is of great fortunate that we could find such kind of matrices. One of the examples is given below:

$$U = \begin{pmatrix} 1 & 0 & 0 \\ 0 & \frac{1}{\sqrt{2}} & \frac{1}{\sqrt{2}} \\ 0 & -\frac{1}{\sqrt{2}} & \frac{1}{\sqrt{2}} \end{pmatrix} \qquad (5.10)$$

where $UU^{-1} = \mathbb{1}$ is trivial to verify.

We denote that:

$$M_{k_x} = \begin{pmatrix} 0 & -1 & 1 \\ -1 & 0 & 0 \\ 1 & 0 & 0 \end{pmatrix}$$

$$M_{k_y} = \begin{pmatrix} 0 & -i & i \\ -i & 0 & 0 \\ i & 0 & 0 \end{pmatrix}$$

$$M_{t_3} = \begin{pmatrix} 0 & & \\ & 1 & \\ & & -1 \end{pmatrix} \tag{5.11}$$

and then it is easy to find that, using Eq. (5.10):

$$\frac{1}{2} k_x \cdot U^{-1} M_{k_x} U = -\frac{\sqrt{2}}{2} k_x \cdot \lambda_1$$

$$\frac{1}{2} k_y \cdot U^{-1} M_{k_y} U = -\frac{\sqrt{2}}{2} k_x \cdot \lambda_5$$

$$U^{-1}\left(-\mathbb{1} + 8t_3 \cdot M_{t_3}\right) U = U^{-1} \cdot U + 8t_3 \cdot U^{-1} M_{t_3} U$$

$$= -\mathbb{1} + 8t_3 \cdot \lambda_6 \tag{5.12}$$

Since the identity operator does not add anything but shift to the Hamiltonian, thus a shift in band structure, we could then rewrite the eigenvalue problem of the Hamiltonian $\hat{\mathcal{H}}$ from Eq. (5.6) into the following Dirac-like equation form:

$$\left(-\mathbb{1} + p_x \lambda_1 + p_y \lambda_5 + \Delta \lambda_6\right) \psi = E\psi \tag{5.13}$$

Note that here we let:

$$p_x = -\frac{\sqrt{2}}{2} k_x, \quad p_y = \frac{\sqrt{2}}{2} k_y, \quad \Delta = 8t_3 \tag{5.14}$$

Eq. (5.13) is the so-called "Dirac-like equation" for calculating the edge states of the system.

Instead of solving this equation to get edge states, what we are going to do in the next section is to calculate the Chern number. In principle we could use this equation to solve for the edge states, but because of some issues with boundary conditions it is simpler to use the direct method of Chapter 5.5 where we plot the eigenvalues of the Hamiltonian numerically in order to obtain edge states.

5.4 Berry curvature and Chern number in the band model

We will take a leave from the last section on elaborating and studying on the Dirac-like equation, and move on to exploring the existence of edge states. This important

idea should have come right before the last chapter, but we hereby explain it in detail, and there is more non-trivial and exotic physics behind it.

5.4.1 Calculation of Berry curvature and Chern number

We begin by first calculating the Berry curvature, which is already mentioned in Chapter 4. From Eq. (3.7), we can easily calculate the Berry curvature of the system as follows:

From Eq. (5.13), we let:

$$\hat{\mathcal{H}}_{eff} = p_x\lambda_1 + p_y\lambda_5 + \Delta\lambda_6 \tag{5.15}$$

as the effective Hamiltonian obtained from $\mathbf{k} \cdot \mathbf{p}$ theory. We then obtained the eigenvalues and their corresponding eigenvectors from it in Table. 5.2. The detailed form of $\hat{v}_2$ and $\hat{v}_3$ complicated to show here. Using Eq. (3.7), we can get the Berry

Table 5.2: Eigensystem of the effective Hamiltonian

Eigenvalue	Eigenvector
0	$\hat{v}_1$
$-\sqrt{p_x^2 + p_y^2 + \Delta^2}$	$\hat{v}_2$
$\sqrt{p_x^2 + p_y^2 + \Delta^2}$	$\hat{v}_3$

curvature with respect to $\hat{v}_2$:

$$\begin{aligned}
\mathcal{F}_2 &= -\mathrm{i}\left(\langle\partial_{k_x}\hat{v}_2|\partial_{k_y}\hat{v}_2\rangle - \langle\partial_{k_y}\hat{v}_2|\partial_{k_x}\hat{v}_2\rangle\right) \\
&= -\frac{\Delta}{\left(p_x^2 + p_y^2 + \Delta^2\right)^{\frac{3}{2}}}
\end{aligned} \tag{5.16}$$

Similarly, we have the Berry curvature with respect to $\hat{v}_3$:

$$\begin{aligned}
\mathcal{F}_3 &= -\mathrm{i}\left(\langle\partial_{k_x}\hat{v}_3|\partial_{k_y}\hat{v}_3\rangle - \langle\partial_{k_y}\hat{v}_3|\partial_{k_x}\hat{v}_3\rangle\right) \\
&= \frac{\Delta}{\left(p_x^2 + p_y^2 + \Delta^2\right)^{\frac{3}{2}}}
\end{aligned} \tag{5.17}$$

Now if we take Eq. (5.17) and integrate it over the whole Brillouin zone, we can thus obtained the Chern number for the band structure in $\frac{1}{5}$-depleted square lattice:

$$
\begin{aligned}
c &= \frac{1}{2\pi} \int_o^\infty dp^2 \cdot \mathcal{F}_3 \\
&= \frac{1}{2\pi} \int_o^\infty dp^2 \cdot \left[\frac{\Delta}{\left(p_x^2 + p_y^2 + \Delta^2\right)^{\frac{3}{2}}} \right] \\
&= 1 \cdot sgn(\Delta)
\end{aligned}
\tag{5.18}
$$

This is the Chern number for one spin species (the spin Chern number). The fact that $c = 1$ clearly indicates that there is one gapless chiral edge state between two bands, which means that the $\frac{1}{5}$-depleted square lattice is a topological insulator.

The detailed procedures to calculate the Chern number for our band structure in $\frac{1}{5}$-depleted square lattice is enclosed in Appendix A. But right now we will move back to the two-band model and discuss about the physics behind its Berry curvature and Chern number.

5.4.2 Berry curvature and band structure of two and three band model

We will discuss about the two-band model here, and calculate its Berry curvature. Then we will compare the results with these from the three-band model. The elaboration on the two-band model is basically based on [30].

We begin with a general Hamiltonian in the space of two orbitals per unit-cell, neglecting that an overall shift of the energy which will not affect the Berry phase as well as assuming that there is no basis of the Bravais lattice,

$$
\hat{\mathcal{H}}_{2b} = \mathbf{k} \cdot \vec{\sigma} + \sigma^z \cdot \Delta
\tag{5.19}
$$

where $\mathbf{k}$ is the momentum, and $\vec{\sigma} = (\sigma_x, \sigma_y, \sigma z)$ are Pauli matrices.

One could easily calculated the Berry curvature from Eq. (5.19):

$$
\mathcal{F} = \pm \frac{1}{2} \cdot \frac{\Delta}{\left(k_x^2 + k_y^2 + \Delta^2\right)^{\frac{3}{2}}}
\tag{5.20}
$$

As is known from [18], Eq. (5.19) looks rather similar to the effective Hamiltonian for graphene, one typical two dimensional topological insulator. For the chiral edge state, the Chern number for graphene is also 1. If we compare both the band structures of $\frac{1}{5}$-depleted square lattice in Fig. 4.5 and those of the graphene case, we may see that there is only one Dirac cone for $\frac{1}{5}$-depleted square lattice in the Brillouin zone but two Dirac cones for graphene. The physics behind this phenomenon is that every cone is associated with the Berry curvature, which contributes equally to the Chern number upon the integration. Thus, for one cone from $\frac{1}{5}$-depleted square lattice, the prefactor is just "1". For two cones from graphene, the prefactor would be divided equally and renders a factor $1/2$.

5.4.3   The three-band model with $SU(2)$ representation

We already knew the well known result [31] that the Chern number of a two band model is equivalent to the winding number of the mapping from a 2D Brillouin zone which is 2D torus (T^2) to the 2D unit sphere (S^2), which is shown in Eq. (5.18). Also, in [30] the relation between the Chern number and winding number for spin-$\frac{1}{2}$ and 1 representation of $SU(2)$ for any integer n with $n \times n$ matrices. We could actually do the same elaboration for our case and extend this notion to the Gell-Mann matrices (2+1 dimensional matrices). As the effective Hamiltonian is given by Eq. (5.15). From Eq. (5.5) and Table. 5.1, the commutation ralation reads:

$$[\lambda_1, \lambda_6] = -2\mathrm{i} f_{156} \cdot \lambda_5 \tag{5.21}$$

where $f_{156} = \frac{1}{2}$. Thus, we have:

$$[\lambda_1, \lambda_6] = \mathrm{i} \cdot \lambda_5 \tag{5.22}$$

which is very similar to $SU(2)$ momentum relation $[J_i, J_j] = \mathrm{i}\epsilon_{ijk} J_k$. Thus we may obtain the eigenvalues are: $E_i/P = -n/2, -(n/2 - 1), ..., n/2 - 1, n/2$ where $P = \sqrt{p_x^2 + \Delta^2 + p_y^2}$. Then for the ith band, we have, if we write in the exterior differential form as:

$$c = -\frac{\mathrm{i}}{2\pi} \int d\psi^\dagger \wedge d\psi \tag{5.23}$$

where ψ is the eigenvector of the renormalised effective Hamiltonian.

Here, we have $n = 2$ for spin-$n/2$ representation, and we have three generalised eigenvalues: $+1, 0, -1$. Thus, we hereby obtain the spin-1 representation of $SU(2)$ for any integer n with respect to $n + 1$ dimensional matrices.

In conclusion, we studied on the relation of Berry curvature and Chern number as well as its physical interpretation in this section, and proved that the $\frac{1}{5}$-depleted square lattice is a kind of topological insulator. We will move on to the next section discussing another important result: the edge state.

5.5   Numerical calculation of the edge states

We can finally take a look at the mysterious edge state of this topological insulator now. Here we discuss the same procedure using the tight-binding Hamiltonian from [18]. To see how these edge states exist, we consider the system setup in Chapter 4, with only the x direction of the lattice going to infinity, and we only consider the intrinsic spin-orbit coupling here since its effect on the band structure is adequate enough.

From Eq. (4.20), we do the usual Fourier Transformation of each operator only with respect to the x direction in k space. Basically, we can then rewrite the Hamiltonian $\hat{\mathcal{H}}$ in the form of bra and ket. The Schrödinger Equation becomes:

$$\hat{\mathcal{H}}^{1P} |\mu, k_x, \sigma\rangle = E_{\mu, k_x} |\mu, k_x, \sigma\rangle \tag{5.24}$$

where σ represents the spin.

For simplicity, we neglect the k_x and σ and make the ansatz of the wavefunction of the solution to Eq. (5.24) as:

$$|\mu\rangle = \sum_n \left[\alpha\,(n)\,|a, n\rangle + \beta\,(n)\,|b, n\rangle + \gamma\,(n)\,|c, n\rangle + \delta\,(n)\,|d, n\rangle\right] \tag{5.25}$$

where $\alpha\,(n)$, $\beta\,(n)$, $\gamma\,(n)$, $\delta\,(n)$ correspond to each position within the primitive cell of the $\frac{1}{5}$-depleted square lattice (A,B,C,D). We plug Eq. (5.25) back into Eq. (5.24), and then compare these coefficients in front of each eigenstate. We could get a group of equations as follows:

$$E \cdot \alpha(n) - (t_1 - 2it_3e^{-ik_x}) \cdot \delta(n) - t_2e^{-ik_x} \cdot \gamma(n) - it_3\beta(n+1) =$$
$$(t_1 + 2it_3e^{-ik_x}) \cdot \beta(n) - it_3\delta(n-1)$$
$$(t_1 - 2it_3e^{ik_x}) \cdot \alpha(n) + (t_1 + 2it_3e^{-ik_x})\gamma(n) =$$
$$E \cdot \beta(n) - t_2\delta(n-1) + it_3\alpha(n-1) - it_3\gamma(n-1)$$
$$E\gamma(n) - (t_1 + 2it_3e^{ik_x})\delta(n) - t_2 \cdot e^{ik_x}\alpha(n) + it_3 \cdot \beta(n+1) =$$
$$(t_1 - 2it_3e^{ik_x}) \cdot \beta(n) + it_3 \cdot \delta(n-1)$$
$$E\delta(n) - (t_1 - 2it_3e^{-ik_x}) \cdot \gamma(n) - t_2 \cdot \beta(n+1) =$$
$$(t_1 + 2it_3e^{ik_x})\alpha(n) + it_3\alpha(n+1) - it_3\gamma(n+1) \tag{5.26}$$

But the situations are a little bit different when it comes to the low edge and the top edge, since there are some coefficients that are zero there.

As shown in Fig. 5.1, we start the layer from $n = 1$. We will set $(t_1, t_2) = (1.0, 1.0)$, and $t_3 = 0.3$ where $k_x \in [-\pi/2, \pi/2]$. At this layer, the boundary condition becomes:

$$E\alpha(1) = (t_1 + 2it_3e^{-ik_x}) \cdot \beta(1) + (t_1 - 2it_3e^{-ik_x}) \cdot \delta(1) + t_2e^{-ik_x} \cdot \gamma(1) + it_3\beta(2)$$
$$E\beta(1) = (t_1 - 2it_3e^{ik_x}) \cdot \alpha(1) + (t_1 + 2it_3e^{-ik_x})\gamma(1)$$
$$E\gamma(1) = (t_1 - 2it_3e^{ik_x})\beta(1) + t_2 \cdot e^{ik_x}\alpha(1) + (t_1 + 2it_3e^{ik_x})\delta(1) - it_3\beta(2)$$
$$E\delta(1) = (t_1 + 2it_3e^{ik_x})\alpha(1) + it_3\alpha(2) - it_3\gamma(2) + (t_1 - 2it_3e^{-ik_x})\gamma(1) + t_2\beta(2) \tag{5.27}$$
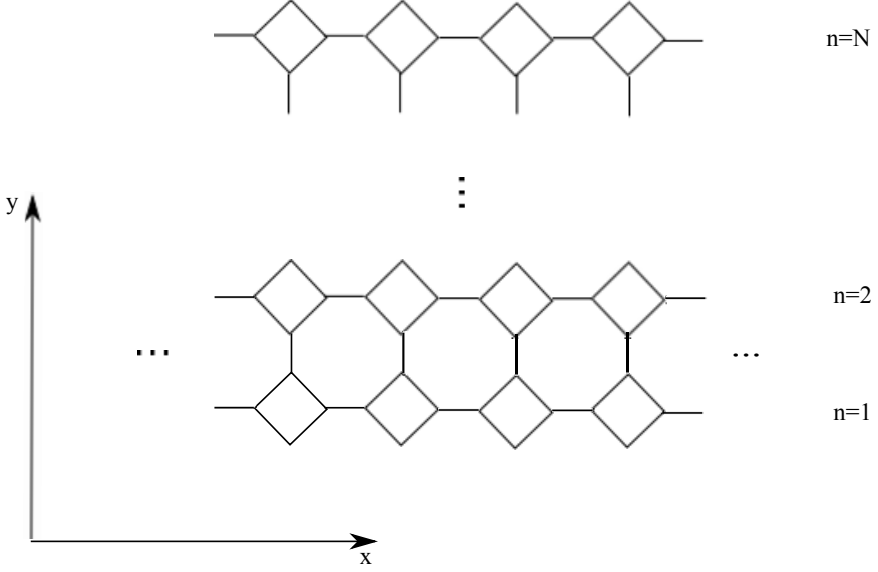
Figure 5.1: Implication of the two-sided edges in $\frac{1}{5}$-depleted square lattice

while on the other hand when it is at the upper boundary, we have:

$$E\alpha(N) = (t_1 + 2\mathrm{i}t_3\mathrm{e}^{-\mathrm{i}k_x}) \cdot \beta(1) + (t_1 - 2\mathrm{i}t_3\mathrm{e}^{-\mathrm{i}k_x}) \cdot \delta(N) + t_2\mathrm{e}^{-\mathrm{i}k_x} \cdot \gamma(N) - \mathrm{i}t_3\delta(N-1)$$

$$E\beta(N) = (t_1 - 2\mathrm{i}t_3\mathrm{e}^{\mathrm{i}k_x}) \cdot \alpha(N) + (t_1 + 2\mathrm{i}t_3\mathrm{e}^{-\mathrm{i}k_x})\gamma(N) + t_2\delta(N-1)$$
$$\qquad - \mathrm{i}t_3\alpha(N-1) + \mathrm{i}t_3\gamma(N-1)$$

$$E\gamma(N) = (t_1 - 2\mathrm{i}t_3\mathrm{e}^{\mathrm{i}k_x})\beta(N) + t_2 \cdot \mathrm{e}^{\mathrm{i}k_x}\alpha(N) + (t_1 + 2\mathrm{i}t_3\mathrm{e}^{\mathrm{i}k_x})\delta(N) + \mathrm{i}t_3\delta(N-1)$$

$$E\delta(N) = (t_1 + 2\mathrm{i}t_3\mathrm{e}^{\mathrm{i}k_x})\alpha(N) + \mathrm{i}t_3\alpha(2) - \mathrm{i}t_3\gamma(N) \qquad\qquad (5.28)$$

Now it is ready to solve for the band structure numerically. We could write all the equations above into the relation of matrices as follows, and then solve and plot the eigenvalue of the matrix $\hat{\mathcal{M}}$, with each point representing a $\pi/50$ step interval

increase:

$$
\begin{pmatrix}
\alpha(1) \\
\beta(1) \\
\gamma(1) \\
\delta(1) \\
\alpha(2) \\
\beta(2) \\
\gamma(2) \\
\delta(2) \\
. \\
. \\
. \\
\alpha(N) \\
\beta(N) \\
\gamma(N) \\
\delta(N)
\end{pmatrix}
= \hat{\mathcal{M}} \cdot
\begin{pmatrix}
\alpha(1) \\
\beta(1) \\
\gamma(1) \\
\delta(1) \\
\alpha(2) \\
\beta(2) \\
\gamma(2) \\
\delta(2) \\
. \\
. \\
. \\
\alpha(N) \\
\beta(N) \\
\gamma(N) \\
\delta(N)
\end{pmatrix}
\tag{5.29}
$$

Finally, we could get the result of edge states in $\frac{1}{5}$-depleted square lattice shown in Fig. 5.2. We set $N = 100$, thus the "layer" of the matrix $\hat{\mathcal{M}}$ to be $\times 100 = 400$, and choose this from 100 bands simulated, and the red and blue lines in the result clearly indicate there are two edge states in this two-sided topological insulator right between the gap in the band structure. We also merge the result together with the bulk bands where each band is equally spaced with a stepwise of $\pi/50$ in the k_y direction in Fig. 5.2b for comparison, showing that the edge states we obtained from numerical simulations are within the third and forth band of the bulk bands.
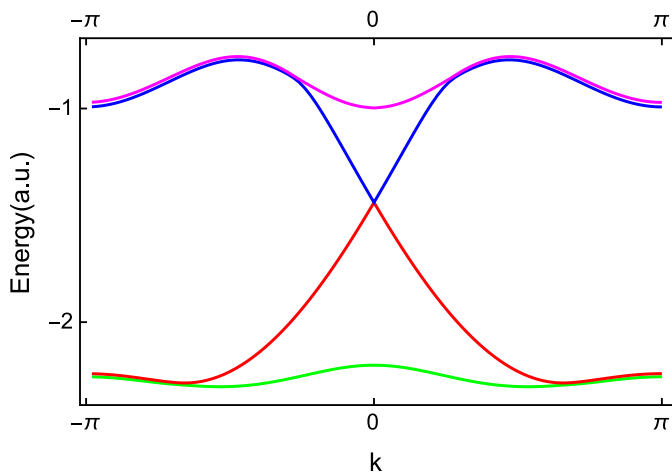
(a) Edge states with $(t_1, t_2) = (1.0, 1.0)$
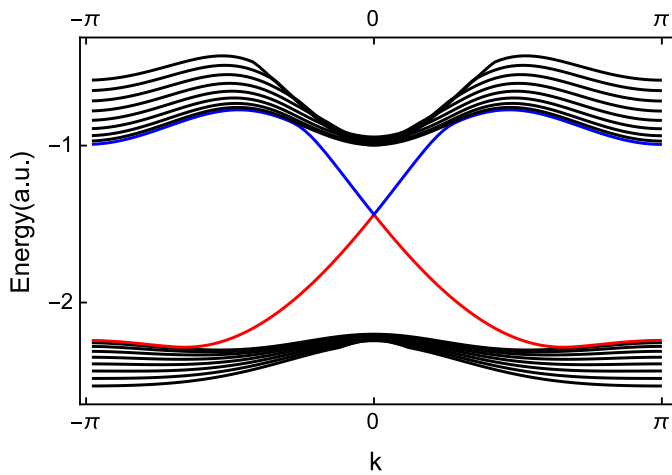
(b) Edge states merged with bulk bands (black lines)

Figure 5.2: Edge states in the $\frac{1}{5}$-depleted square lattice

Chapter 6

Non-symmorphic symmetry and degeneracies

As the final chapter of the thesis, we would like to study the non-symmorphic symmetry in our system. We here followed by the idea taken from [1] for non-symmorphic symmetry in the $\frac{1}{5}$-depleted square lattice .

6.1 Non-symmorphic symmetry in the $\frac{1}{5}$-depleted square lattice induced by spins

In the previous part of thesis, we mentioned that the $\frac{1}{5}$-depleted square lattice has C_{4v} symmetry. In order to obtain more information of non-symmorphic symmetry, one may increase the lattice's degree of freedom. Here, we could abandon the four-atom primitive cell and focus on the eight-atom primitive cell, shown in Fig. 6.1.

Notice that we also did the rotation of the coordinate axes for $\pi/4$ degrees. The distance between the nearest-neighbor primitive cell is a. For our convenience of discussion below, we set $a = 1$.

For the non-symmorphic symmetry, as introduced in Chapter 3, we essentially need to find the non-symmorphic space groups which are distinguished by the existence of symmetry operations that combine point group operations g with translations t that are a fraction of a Bravais lattice vector. We will perform our searching by placing electrons with either spin up (denoted by nothing) or spin down (denoted by a crossing in a circle) on the lattice. This can also be generated physically by puckering as discussed in [1].

Here we show two examples which satisfy the non-symmorphic symmetry. In order to illustrate this in a intuitive way, we first label each atom in one primitive cell from ① to ⑧ as in Fig. 6.2. Also, we denote the four-component row vector
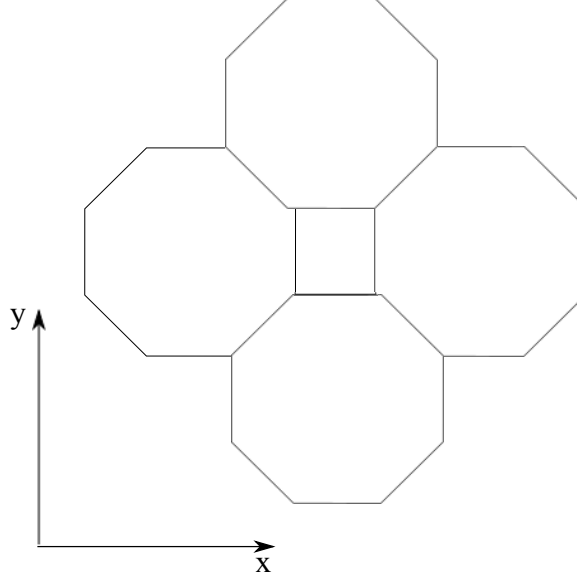
Figure 6.1: Schematics of eight-atom primitive cell

such as $(1, 2, 3, 4) = (-1, -1, -1, -1)$ as putting the four spin down electrons at the position No. $1, 2, 3$ and 4 while the rest four are all spin up electrons.

Then we could show that the two cases are $(1, 2, 3, 8) = (-1, -1, -1, -1)$ and $(1, 6, 7, 8) = (-1, -1, -1, -1)$, which are depicted in Fig. 6.3.

Notice that the screw axis (red dotted line) in both figures are behaved as flipping along it, thus changing the spins of the electrons (up to down, and down to up). Also, the $g = C_{2\hat{x}}$ and $g = C_{2\hat{y}}$ are satisfied with the fact that $g\mathbf{t} = \mathbf{t}$. In both of our case, $\mathbf{t}$ is the half translation of coordinate k_x or k_y. This is denoted as $\{g|\mathbf{t}\}$. We will see in the next section that a non-symmorphic symmetry $\{g|\mathbf{t}\}$ still protects degeneracies in the invariant line or plane in the BZ that satisfies $g\mathbf{k} = \mathbf{k}$. We will discuss more on it for details in the next section.

6.2   Band structure protected by non-symmorphic symmetry

For the lattice expanded both in x and y direction in two dimension, we just simply follow the procedures similar to those specified in Chapter 3. We write down the Hamiltonian of the model as follows:

$$\hat{\mathcal{H}} = \sum_{i,j} H_{ij} c_{ni}^{\dagger} c_{nj} + h.c. \tag{6.1}$$
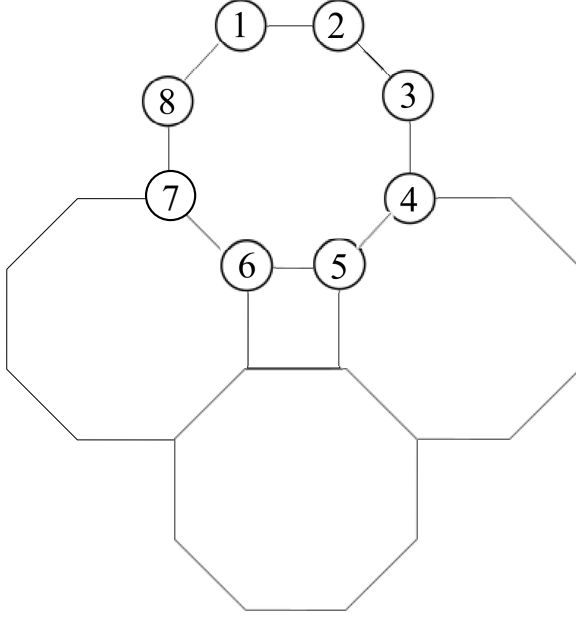
Figure 6.2: Labeling of eight-atom primitive cell

where *h.c.* stands for Hermitian conjugate.

After the Fourier transformation, we will have an 8×8 matrix for the whole system shown below.

$$
H_{i,j} =
\begin{pmatrix}
0 & t_1 & 0 & 0 & 0 & t_1 e^{ik_y} & 0 & t_2 \\
t_1 & 0 & t_2 & 0 & t_1 e^{ik_y} & 0 & 0 & 0 \\
0 & t2 & 0 & t1 & 0 & 0 & 0 & t_1 e^{ik_x} \\
0 & 0 & t_1 & 0 & t_2 & 0 & t_1 e^{ik_x} & 0 \\
0 & t_1 e^{-ik_y} & 0 & t_2 & 0 & t_1 & 0 & 0 \\
t_1 e^{-ik_y} & 0 & 0 & 0 & t_1 & 0 & t_2 & 0 \\
0 & 0 & 0 & t_1 e^{-ik_x} & 0 & t_2 & 0 & t_1 \\
t_2 & 0 & t_1 e^{-ik_x} & 0 & 0 & 0 & t_1 & 0
\end{pmatrix}
$$

$$(6.2)$$

We essentially solve the eigenvalue problem for Eq. (6.2), of which the values are the energy spectrum, thus the band structure.

Now we need to consider the non-symmorphic factor into the whole system. We realise this by simply introducing a $\pm\delta$ term added into the diagonal components of the Hamiltonian. This could be physically considered as an additional $\pm\delta c^{\dagger}_{ni} c_{ni}$ term added into the Hamiltonian in Eq. (6.1), which could be some small magnetic

(a) $(1, 2, 3, 8) = (-1, -1, -1, -1)$ **(b)** $(1, 6, 7, 8) = (-1, -1, -1, -1)$
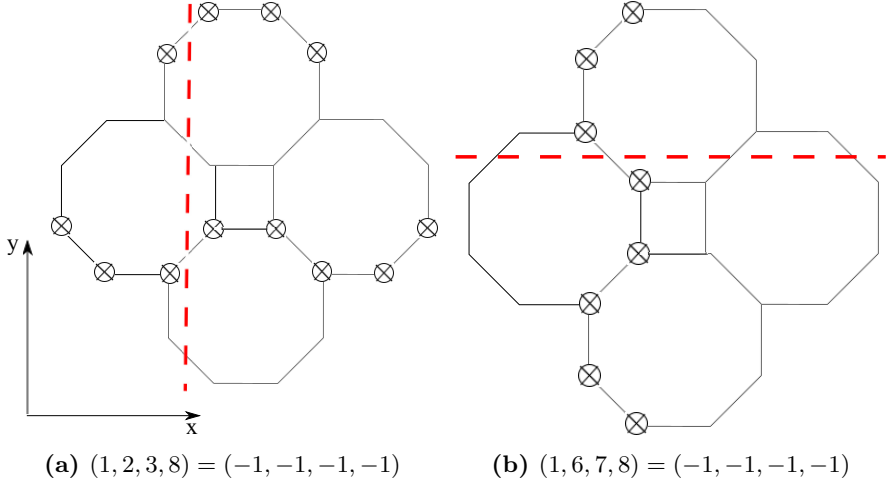
Figure 6.3: Non-symmorphic symmetry in the $\frac{1}{5}$-depleted square lattice

field perturbation. We will then observe how the band structure react to it with respect to the non-symmorphic symmetry.

We put $\delta = 0.5$. From Fig. 6.4, we see that the non-symmorphic symmetry of the lattice will essentially protect the degeneracies of the band structure either from X to M, which is along the k_y direction, or from M to Σ, which is along the $-k_x$ direction in BZ. This result is also consistent with the fact that $g\mathbf{k} = \mathbf{k}$ for non-symmorphic symmetry in the previous section.

(a) No spin-orbit coupling

(b) Symmorpihc symmetry

(c) $(1, 2, 3, 8) = (-1, -1, -1, -1)$

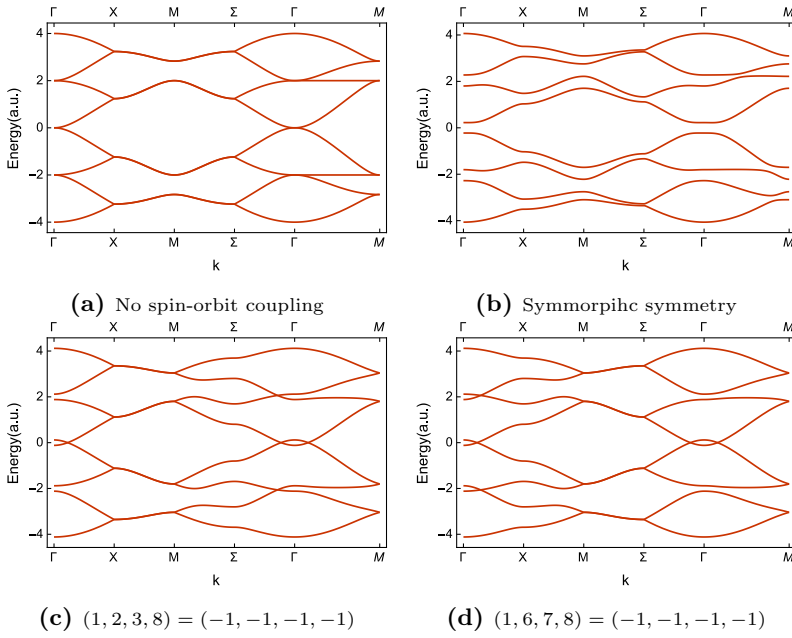**(d)** $(1, 6, 7, 8) = (-1, -1, -1, -1)$

Figure 6.4: Dispersion relations with/without non-symmorphic symmetry where $t_2 = 2t_1$

Part III

Conclusion and Discussion

Chapter 7

Summary

In conclusion, we have focused on studying the topological edge state of an interesting lattice model: $\frac{1}{5}$-depleted square lattice in the thesis. Most of our work is based on and continued from [22] from the perspective of topological insulator within the framework of band structure theory as well as tight-binding models. We added both intrinsic and Rashba spin-orbit coupling into the tight-binding Hamiltonian and found out how it will relieve the degeneracies around the highly symmetric Dirac points in the band structure. The Dirac-like equation for direct solutions to the chiral edge states of the lattice is also derived using $\mathbf{k} \cdot \mathbf{p}$ method and the edge states were obtained numerically. In addition, we find that the number of Dirac cones in the Brillouin zone is closely related to the Berry curvatures by comparing the difference between two band and three band models. Also, the non-symmorphic symmetry of the lattice is studied by physically generating the spin configuration by puckering the lattice as discussed in [1].

However, there are still many aspects of the topic to be further studied and elaborated. One straight mission to be done is to take a look at the band structure and compare it with the results in our thesis if we consider eight-atom primitive cells in the lattice by adding either intrinsic spin-orbit coupling or Rashba spin-orbit coupling into the Hamiltonian. Another very important question is trying to obtain the solution of the edge state directly from the Dirac-like equation itself rather than numerical methods we used in the thesis. This requires a careful treatment of the boundary conditions.

Appendix A

Detailed calculation of Chern number

We have the expression of Berry curvature as:

$$\mathcal{F}\left(p_x, p_y\right) = \frac{\Delta}{\left(p_x^2 + p_y^2 + \Delta^2\right)^{\frac{3}{2}}} \tag{A.1}$$

where we made the following notations:

$$p_x = -\frac{\sqrt{2}}{2} k_x, \quad p_y = \frac{\sqrt{2}}{2} k_y \tag{A.2}$$

Then Eq. (A.1) will become:

$$\mathcal{F}\left(k_x, k_y\right) = \frac{\sqrt{2}\Delta}{\left(k_x^2 + k_y^2 + 2\Delta^2\right)^{\frac{3}{2}}} \tag{A.3}$$

Note that here we do the the transformation between two Berry curvatures but they are essentially the same if we integrate them separately with respect to different variables.

Let

$$k_x = r \cos(\theta), \quad k_y = r \sin(\theta), \tag{A.4}$$

where $r \in [0, +\infty)$ and $\theta \in [0, 2\pi]$.

Then we calculate the Chern number as follows:

$$c = \frac{1}{2\pi} \int dk^2 \cdot \mathcal{F}$$

$$= \frac{1}{2\pi} \int_0^{2\pi} d\theta \int_0^{+\infty} r \cdot dr \left(\frac{\sqrt{2}\Delta}{\left(k_x^2 + k_y^2 + 2\Delta^2\right)^{\frac{3}{2}}} \right)$$

$$= \frac{1}{2\pi} \cdot 2\pi \int_0^{+\infty} \frac{1}{2} \cdot dr^2 \cdot \left(\frac{\sqrt{2}\Delta}{\left(r^2 + 2\Delta^2\right)^{\frac{3}{2}}} \right)$$

$$= \frac{1}{2} \int_0^{+\infty} dr^2 \cdot \frac{\sqrt{2}\Delta}{\left(r^2 + 2\Delta^2\right)^{\frac{3}{2}}} = \{t = r^2\}$$

$$= \frac{1}{2} \int_0^{+\infty} dt \cdot \frac{\sqrt{2}\Delta}{\left(t + 2\Delta^2\right)^{\frac{3}{2}}}$$

$$= -\sqrt{2}\Delta \cdot \left[0 - \frac{1}{\sqrt{2}\Delta} \right] = 1 \cdot sgn(\Delta) \tag{A.5}$$

It is trivial to see that the Chern number is ± 1. Since this is a topological invariant, it does not care about the size of Δ, only the sign that matters.

Appendix B

Matlab code for the calculation of edge states

Here we append the Matlab code for numerical calculation of the edge states in the $\frac{1}{5}$-depleted square lattice with intrinsic spin-orbit couplings.

```matlab
%% Generate a N—dimensional matrix which is used for recursion formula of edge states
clc
clear all

% Define parameter
N = 25; %number of layers of the lattice
M = zeros(4*N); %create an all—zero N*N matrix
t1 = 1.0;
t2 = 1.0;
t3 = 0.3; %constants from the Hamiltonian
%t2=0
%t3=0

step=100;%total footsteps of kx value
delta_kx=2*pi/step;%intervals of kx value
%kx=—pi/2; %initial value of kx value

kx = —pi;

res=zeros(4*N,step);% the result recording matrix
% Generate the complete matrix
%The first layer, i.e. the boundary condition


%% Calculate the eigenvalue of the matrix

% Display setting for the screen print
%name = 'Alice';
```

```matlab
30  %age = 12;
31  %ponsn = ['Calculating the number ',num2str(l),' eigenvalue now.'];
32  %disp(ponsn)
33
34  % Loop for discretized kx value from −pi to +pi and record the data
35  %l=1;
36  for l=1:step
37  kx=−pi+delta_kx*l;
38  %M=newmat(kx);
39
40  %%%%%%%%%%%%%%%%%%%%%%%%%%%%Renewing the M matrix %%%%%%%%%%%%%%%%%%%%%%%%%
41  M(1,2)=t1+1*1i*t3*exp(−1i*kx);
42  M(1,4)=t1−1*1i*t3*exp(−1i*kx);
43  M(1,3)=t2*exp(−1i*kx);
44  M(1,6)=1i*t3;
45
46  M(2,1)=t1−1*1i*t3*exp(1i*kx);
47  M(2,3)=t1+1*1i*t3*exp(−1i*kx);
48
49  M(3,2)=t1−1*1i*t3*exp(1i*kx);
50  M(3,1)=t2*exp(1i*kx);
51  M(3,4)=t1+1*1i*t3*exp(1i*kx);
52  M(3,6)=−1i*t3;
53
54  M(4,1)=t1+1*1i*t3*exp(1i*kx);
55  M(4,5)=1i*t3;
56  M(4,7)=−1i*t3;
57  M(4,3)=t1−1*1i*t3*exp(−1i*kx);
58  M(4,6)=t2;
59
60  %The last layer, i.e. the upward boundary
61  M(4*(N−1)+1,4*(N−1)+4)=t1−1*1i*t3*exp(−1i*kx);
62  M(4*(N−1)+1,4*(N−1)+3)=t2*exp(−1i*kx);
63  M(4*(N−1)+1,4*(N−1)+2)=t1+1*1i*t3*exp(−1i*kx);
64  M(4*(N−1)+1,4*(N−2)+4)=−1i*t3;
65
66  M(4*(N−1)+2,4*(N−1)+1)=t1−1*1i*t3*exp(1i*kx);
67  M(4*(N−1)+2,4*(N−1)+3)=t1+1*1i*t3*exp(−1i*kx);
68  M(4*(N−1)+2,4*(N−2)+4)=t2;
69  M(4*(N−1)+2,4*(N−2)+1)=−1i*t3;
70  M(4*(N−1)+2,4*(N−2)+3)=1i*t3;
71
72  M(4*(N−1)+3,4*(N−1)+4)=t1+1*1i*t3*exp(1i*kx);
73  M(4*(N−1)+3,4*(N−1)+1)=t2*exp(1i*kx);
74  M(4*(N−1)+3,4*(N−1)+2)=t1−1*1i*t3*exp(1i*kx);
75  M(4*(N−1)+3,4*(N−2)+4)=1i*t3;
76
77  M(4*(N−1)+4,4*(N−1)+1)=t1+1*1i*t3*exp(1i*kx);
78  M(4*(N−1)+4,4*(N−1)+3)=t1−1*1i*t3*exp(−1i*kx);
79
80  %The rest entries of the bulk
81
82  for n=2:N−1
83  M(4*(n−1)+1,4*(n−1)+4)=t1−1*1i*t3*exp(−1i*kx);
84  M(4*(n−1)+1,4*(n−1)+3)=t2*exp(−1i*kx);
```

```
85   M(4*(n−1)+1,4*(n−1)+2)=t1+1*1i*t3*exp(−1i*kx);
86   M(4*(n−1)+1,4*(n−2)+4)=−1i*t3;
87   M(4*(n−1)+1,4*n+2)=1i*t3;
88
89   M(4*(n−1)+2,4*(n−1)+1)=t1−1*1i*t3*exp(1i*kx);
90   M(4*(n−1)+2,4*(n−1)+3)=t1+1*1i*t3*exp(−1i*kx);
91   M(4*(n−1)+2,4*(n−2)+4)=t2;
92   M(4*(n−1)+2,4*(n−2)+1)=−1i*t3;
93   M(4*(n−1)+2,4*(n−2)+3)=1i*t3;
94
95   M(4*(n−1)+3,4*(n−1)+4)=t1+1*1i*t3*exp(1i*kx);
96   M(4*(n−1)+3,4*(n−1)+1)=t2*exp(1i*kx);
97   M(4*(n−1)+3,4*(n−1)+2)=t1−1*1i*t3*exp(1i*kx);
98   M(4*(n−1)+3,4*(n−2)+4)=1i*t3;
99   M(4*(n−1)+3,4*n+2)=−1i*t3;
100
101  M(4*(n−1)+4,4*(n−1)+1)=t1+1*1i*t3*exp(1i*kx);
102  M(4*(n−1)+4,4*(n−1)+3)=t1−1*1i*t3*exp(−1i*kx);
103  M(4*(n−1)+4,4*n+2)=t2;
104  M(4*(n−1)+4,4*n+1)=1i*t3;
105  M(4*(n−1)+4,4*n+3)=−1i*t3;
106  end
107  %%%%%%%%%%%%%%%%%%%%%%%%%%%%%%%%%%%%%%%%%%%%%%%%%%%%%%%%%%%%%%%%%%%%%%%%%%
108  res(:,l)=eig(M);
109  % Display setting for the screen print
110  %name = 'Alice';
111  %ll = l;
112  ponsn = ['Calculating the number ',num2str(l),' eigenvalue now.'];
113  disp(ponsn)
114  end
115
116  disp('End of the eigenvalue calculation and recording.')
117  % Calculatee the absolute value of the eigenvalues
118  %Abs_res=abs(res);
119  disp('End of calculating eigenvalue data.')
120
121  %% Extract the desired data for edge states to be plotted in Mathematica
122  temp_res=res';
123  temp_data=temp_res(:,17:34);
124  x=−pi+2*pi/100:2*pi/100:pi;
125
126  data17=zeros(100,2);
127  data18=zeros(100,2);
128  data19=zeros(100,2);
129  data20=zeros(100,2);
130  data21=zeros(100,2);
131  data22=zeros(100,2);
132  data23=zeros(100,2);
133  data24=zeros(100,2);
134  data25=zeros(100,2);
135  data26=zeros(100,2);
136  data27=zeros(100,2);
137  data28=zeros(100,2);
138  data29=zeros(100,2);
139  data30=zeros(100,2);
```

```
140  data31=zeros(100,2);
141  data32=zeros(100,2);
142  data33=zeros(100,2);
143  data34=zeros(100,2);
144  %data35=zeros(100,2);
145
146  data17(:,1)=x';
147  data18(:,1)=x';
148  data19(:,1)=x';
149  data20(:,1)=x';
150  data21(:,1)=x';
151  data22(:,1)=x';
152  data23(:,1)=x';
153  data24(:,1)=x';
154  data25(:,1)=x';
155  data26(:,1)=x';
156  data27(:,1)=x';
157  data28(:,1)=x';
158  data29(:,1)=x';
159  data30(:,1)=x';
160  data31(:,1)=x';
161  data32(:,1)=x';
162  data33(:,1)=x';
163  data34(:,1)=x';
164
165  data17(:,2)=temp_data(:,1);
166  data18(:,2)=temp_data(:,2);
167  data19(:,2)=temp_data(:,3);
168  data20(:,2)=temp_data(:,4);
169  data21(:,2)=temp_data(:,5);
170  data22(:,2)=temp_data(:,6);
171  data23(:,2)=temp_data(:,7);
172  data24(:,2)=temp_data(:,8);
173  data25(:,2)=temp_data(:,9);
174  data26(:,2)=temp_data(:,10);
175  data27(:,2)=temp_data(:,11);
176  data28(:,2)=temp_data(:,12);
177  data29(:,2)=temp_data(:,13);
178  data30(:,2)=temp_data(:,14);
179  data31(:,2)=temp_data(:,15);
180  data32(:,2)=temp_data(:,16);
181  data33(:,2)=temp_data(:,17);
182  data34(:,2)=temp_data(:,18);
183
184  data_test=temp_data(:,3)';
185
186  %save('mdata.mat','temp_data'); % save the data as a mat file
187  save('mdata17.mat','data17');
188  save('mdata18.mat','data18');
189  save('mdata19.mat','data19');
190  save('mdata20.mat','data20');
191  save('mdata21.mat','data21');
192  save('mdata22.mat','data22');
193  save('mdata23.mat','data23');
194  save('mdata24.mat','data24');
```

```matlab
195  save('mdata25.mat','data25');
196  save('mdata26.mat','data26');
197  save('mdata27.mat','data27');
198  save('mdata28.mat','data28');
199  save('mdata29.mat','data29');
200  save('mdata30.mat','data30');
201  save('mdata31.mat','data31');
202  save('mdata32.mat','data32');
203  save('mdata33.mat','data33');
204  save('mdata34.mat','data34');
205
206
207  save('test_data.mat','data_test');
208  %% Plot the edge states
209
210  figure,plot(res(17,:))
211  hold on;
212  plot(res(18,:))
213  hold on;
214  plot(res(19,:))
215  hold on;
216  plot(res(20,:))
217  hold on;
218  plot(res(21,:))
219  hold on;
220  plot(res(22,:))
221  hold on;
222  plot(res(23,:))
223  hold on;
224  plot(res(24,:))
225  hold on;
226  plot(res(25,:))
227  hold on;
228  plot(res(26,:))
229  hold on;
230  plot(res(27,:))
231  hold on;
232  plot(res(28,:))
233  hold on;
234  plot(res(29,:))
235  hold on;
236  plot(res(30,:))
237  hold on;
238  plot(res(31,:))
239  hold on;
240  plot(res(32,:))
241  hold on;
242  plot(res(33,:))
243  hold on;
244  plot(res(34,:))
245
246  %  figure, plot(res(25,:))
```

Bibliography

[1] S. M. Young and C. L. Kane, *Dirac Semimetals in Two Dimensions*, Phys. Rev. Lett. **115**, 126803 (2015).

[2] D. J. Thouless *et al.*, *Quantized Hall Conductance in a Two-Dimensional Periodic Potential*, Phys. Rev. Lett. **49**, 405 (1982).

[3] X. G. Wen, *Topological orders and edge excitations in fractional quantum Hall states*, Advances in Physics **44**, 405 (1995).

[4] C. L. Kane and E. J. Mele, *Quantum Spin Hall Effect in Graphene*, Phys. Rev. Lett. **95**, 226801 (2005).

[5] C. L. Kane and E. J. Mele, *Z_2 Topological Order and the Quantum Spin Hall Effect*, Phys. Rev. Lett. **95**, 146802 (2005).

[6] L. Fu, C. L. Kane and E. J. Mele, *Topological Insulators in Three Dimensions*, Phys. Rev. Lett. **98**, 106803 (2007).

[7] J. E. Moore and L. Balents, *Topological invariants of time-reversal-invariant band structures*, Phys. Rev. B **75**, 121306 (2007).

[8] R. Roy, *Topological phases and the quantum spin Hall effect in three dimensions*, Phys. Rev. B **79**, 195322 (2009).

[9] B. A. Bernevig, T. L. Hughes and S. C. Zhang, *Quantum Spin Hall Effect and Topological Phase Transition in HgTe Quantum Wells*, Science **314**, 1757 (2006).

[10] L. Fu and C. L. Kane, *Topological insulators with inversion symmetry*, Phys. Rev. B **76**, 045302 (2007).

[11] M. König *et al.*, *Quantum Spin Hall Insulator State in HgTe Quantum Wells*, Science **318**, 766 (2007).

[12] D. Hsieh *et al.*, *A topological Dirac insulator in a quantum spin Hall phase*, Nature **452**, 970 (2008).

[13] Y. Xia *et al.*, *Observation of a large-gap topological-insulator class with a single Dirac cone on the surface*, Nature Physics **5**, 398 (2009).

[14] H. Zhang *et al.*, *Topological insulators in Bi2Se3, Bi2Te3 and Sb2Te3 with a single Dirac cone on the surface*, Nature physics **5**, 438 (2009).

[15] D. C. Tsui, H. L. Stormer and A. C. Gossard, *Two-Dimensional Magneto-transport in the Extreme Quantum Limit*, Phys. Rev. Lett. **48**, 1559 (1982).

[16] R. B. Laughlin, *Anomalous Quantum Hall Effect: An Incompressible Quantum Fluid with Fractionally Charged Excitations*, Phys. Rev. Lett. **50**, 1395 (1983).

[17] F. Bloch, *Über die quantenmechanik der elektronen in kristallgittern*, Zeitschrift für physik **52**, 555 (1929).

[18] A. H. Castro Neto *et al.*, *The electronic properties of graphene*, Rev. Mod. Phys. **81**, 109 (2009).

[19] H. M. Guo and M. Franz, *Topological insulator on the kagome lattice*, Phys. Rev. B **80**, 113102 (2009).

[20] Z. Meng *et al.*, *Quantum spin liquid emerging in two-dimensional correlated Dirac fermions*, Nature **464**, 847 (2010).

[21] S. Sorella, Y. Otsuka and S. Yunoki, *Absence of a spin liquid phase in the Hubbard model on the honeycomb lattice*, Scientific reports **2** (2012).

[22] Y. Yamashita *et al.*, *SU(3) Dirac electrons in the $\frac{1}{5}$-depleted square-lattice Hubbard model at $\frac{1}{4}$ filling*, Phys. Rev. B **88**, 195104 (2013).

[23] S. Q. Shen, *Topological Insulators: Dirac Equation in Condensed Matters* (Springer Science & Business Media, 2013).

[24] A. Altland and B. D. Simons, *Condensed matter field theory* (Cambridge University Press, 2010).

[25] N. Ashcroft and N. Mermin, *Solid State Physics* (Saunders College, Philadelphia, 1976).

[26] J. J. Sakurai and J. Napolitano, *Modern quantum mechanics* (Addison-Wesley, 2011).

[27] N. M. R. Peres, *Colloquium : The transport properties of graphene: An introduction*, Rev. Mod. Phys. **82**, 2673 (2010).

[28] C. Bradley and A. P. Cracknell, *The Mathematical Theory of Symmetry in Solids: Representation Theory for Points Groups and Space Groups* (Clarendon Press, 1972).

[29] Y. Peter and M. Cardona, *Fundamentals of semiconductors: physics and materials properties* (Springer Science & Business Media, 2010).

[30] Y. He, J. Moore and C. M. Varma, *Berry phase and anomalous Hall effect in a three-orbital tight-binding Hamiltonian*, Phys. Rev. B **85**, 155106 (2012).

[31] X. L. Qi, Y. S. Wu and S. C. Zhang, *Topological quantization of the spin Hall effect in two-dimensional paramagnetic semiconductors*, Phys. Rev. B **74**, 085308 (2006).